Research and Development of a 13-inch Hybrid Avalanche Photo-Detector and its Readout System for a Water Cherenkov Detector

NAKAYAMA Hiroyuki

January 2006

Abstract

A new photo sensor, Hybrid Avalanche Photo-Detector(HAPD) and its dedicated readout system have been developed for next generation water Cerenkov detectors.

We measured the performance of the 13 inch-diameter prototype HAPD. We observed the total gain of $\sim$24,000 and the time resolution of σ=0.7 ns for 1 p.e. Note that this time resolution includes that of the readout system.

A dedicated readout system for the HAPD has also been developed, consisting of 1) an ASIC preamplifier with wide bandwidth and low noise, 2) AMC(Analog Memory Cell) ASIC as a waveform sampling device, and 3) digital filtering algorithm implemented on FPGA. The ASIC preamplifier has the rise time of $\sim$1 ns and the ENC of 3,700 electrons with detector capacitance of 70 pF. The AMC is under development, and our prototype has the sampling speed of $\sim$1 GHz and the depth of 64, Our goal is to achieve the depth of 512$\sim$1024 and the resolution of 10bit. We optimized the digital filtering algorithm to have shorter kernel length, implemented it on FPGA, and estimated the cost.

Contents

Chapter 1

Introduction

In this thesis, we report the evaluation of 13-inch Hybrid Avalanche Photo-Detector (HAPD) and the research and development of the readout system of the HAPD, for next generation water Cherenkov detectors.

The evidence of neutrino oscillation in the atmospheric neutrino was discovered by Super-Kamiokande in 1998[2]. This is the first observation beyond the Standard Model. Since then, neutrino experiments have attracted a great deal of attention in the field of particle physics, and have achieved new results as follows. The oscillation has been confirmed by the first accelerator based long-baseline experiment, K2K, in Japan[3]. Recently, it has shown that the origin of the solar neutrino deficit was also neutrino oscillation, by the solar neutrino experiments and reactor based neutrino oscillation experiments, such as Super-Kamiokande[3, 4], SNO[5, 6], and KamLand[7, 8, 9, 10].

Although the mechanism of neutrino sector is beginning to be understood through these significant results, next generation neutrino experiments are awaited because there is clear limitation to the existing experiments for a full understanding of the sector. There are many neutrino experiments planned and proceeding in the world. Megaton class water Cherenkov detector experiment, such as Hyper-Kamiokande project[11], is one of the planned to overcome the current neutrino oscillation limits and find new physics like proton decay.

The experiment consists of the large water tank and photosensors mounted on the tank walls to detect Cherenkov lights. The current existing photosensors like PMT can not suit the experiment because the number of photosensors needed is quite large ($\sim$200,000) and we can easily expect to face problems of total cost of the experiment and quality control of photosensors.

We believe HAPD is the solution to solve the problems and develop HAPD and its readout system. In 2004, 13-inch diameter HAPD was made available for the first time. HAPD itself has many desirable features like simpler structure, single photon sensitivity, and better time resolution, compared to PMT. However, the dedicated readout system has to be developed to compensate HAPD's gain ($\sim 10^5$), two orders of magnitude lower than that of PMT.

Physics motivation, next generation water Cherenkov detector, and the principle of HAPD are discussed in Section 2. The evaluation of 13-inch HAPD is described in Chapter 2 to show our HAPD satisfies the basic requirements for the next generation water Cherenkov experiments. In Chapter 3, we discuss the development and performance of the readout system, consisting of 1) an ASIC preamplifier, 2) a waveform sampling device, and 3) the digital filtering algorithm. We summarize the study in Chapter 4.

Chapter 2

Neutrino experiments and the target of our R&D

Next generation water Cherenkov detector experiments are desired. However, there are some difficulties in realizing these experiments. We believe HAPD will solve some of the difficulties.

In this chapter, we describe the physics background, difficulties of next generation experiment, and why HAPD can solve the difficulties.

2.1 Neutrino and its oscillation

Neutrino is one of the elementary particles which the Universe is composed of. Since neutrinos don't carry electrical charge and rarely interact with matter, they are the most difficult to detect, compared to other known elementary particles. As a result, they are also the least understood. Except for the electrical charge, neutrinos are similar to charged leptons. The weak force treats neutrinos and charged leptons identically; the strong force affect neither of them; and the gravitational force couples both of them with other massive particles (remember neutrinos are recently proved to have finite masses). There are three types, or "flavors," of neutrinos: electron-neutrino, mu-neutrino, and tau-neutrino. Charged leptons have also three flavors: electron, muon, and tauon, corresponding to each flavor of neutrinos. Neutrinos and charged leptons are categorized to "leptons." There are other types of elementary particles called "quarks" which also have six components, and "gauge bosons" which meditate forces. All the elementary particles are listed in Table 2.1 and Table 2.2.

Neutrino oscillation is the phenomenon that neutrino changes their flavor as they fly. This phenomenon can occur only when neutrinos have finite (non-zero) mass, as explained in the following.

Assuming that neutrinos have finite masses. Neutrino flavor eigenstates (ν_e, ν_μ,

Generation	1	2	3	Electric charge
Neutrinos	ν_e	ν_μ	ν_τ	0
Charged leptons	e	μ	τ	-1
Up-type Quarks	u	c	t	$+\frac{2}{3}$
Down-type Quarks	d	s	b	$-\frac{1}{3}$

Table 2.1: Table of "Leptons" and "Quarks."

Gauge boson	Corresponding force
g (gluon)	Strong force
$W^\pm, Z$ (weak boson)	Weak force
γ (photon)	Electromagnetic force
G? (graviton)	Gravitational force

Table 2.2: Table of "gauge bosons" and corresponding force.

and ν_τ) are written using their mass eigenstates (ν_1, ν_2, and ν_3):

$$\begin{pmatrix} \nu_e \\ \nu_\mu \\ \nu_\tau \end{pmatrix} = \begin{pmatrix} U_{e1} & U_{e2} & U_{e3} \\ U_{\mu1} & U_{\mu2} & U_{\mu3} \\ U_{\tau1} & U_{\tau2} & U_{\tau3} \end{pmatrix} \begin{pmatrix} \nu_1 \\ \nu_2 \\ \nu_3 \end{pmatrix} \tag{2.1}$$

where matrix U is an unitary matrix called "NMS matrix." In free space, the Shrödinger equation of a neutrino is given as follows:

$$i\frac{d}{dt}\nu_i(t) = H_i\nu_i(t)(i = 1, 2, 3) \tag{2.2}$$

using a diagonalized operator matrix H. The solution of the equation is

$$\nu_i(t) = \nu_i(0)e^{-iE_it}(E_i \equiv \sqrt{p_i^2 + m_i^2}) \tag{2.3}$$

where p_i and m_i are the momentum and the mass of ν_i.

For the simplicity, here we consider only two neutrino flavors ν_μ and ν_τ, and two neutrino mass eigenstates ν_2 and ν_3. Then we can rewrite equation 2.1 using a mixing angle θ:

$$\begin{pmatrix} \nu_\mu \\ \nu_\tau \end{pmatrix} = \begin{pmatrix} \cos\theta & \sin\theta \\ -\sin\theta & \cos\theta \end{pmatrix} \begin{pmatrix} \nu_2 \\ \nu_3 \end{pmatrix} \tag{2.4}$$

The time evolution of the waveform function of the neutrino, $\nu(t)$ is given as follows, assuming that $\nu(0) = \nu_\mu$:

$$\begin{aligned} \nu(t) &= \cos\theta\nu_2(t) + \sin\theta\nu_3(t) & (2.5) \\ &= (\cos^2\theta e^{-iE_2t} - \sin^2\theta e^{-iE_3t})\nu_\mu \\ &\quad + \sin\theta\cos\theta(e^{-iE_2t} - e^{-iE_3t})\nu_\tau & (2.6) \end{aligned}$$

Thus, ν_μ which is generated at time 0, can be observed as ν_τ at time t with the possibility $P(\nu_\mu \to \nu_\tau)$ given by:

$$P(\nu_\mu \to \nu_\tau) = \sin^2 2\theta \sin^2((E_3 - E_2)t/2). \tag{2.7}$$

Assuming that $m_i^2 << p_i^2$,

$$P(\nu_\mu \to \nu_\tau) \simeq \sin^2 2\theta \sin^2(\frac{\Delta m^2 t}{2E}). \tag{2.8}$$

where $\Delta m^2 \equiv m_3^2 - m_2^2$ and $E \equiv p_i \simeq E_i$. Therefore, neutrino oscillation can take place only when at least one neutrino have finite (non-zero) mass.

The question whether neutrinos have masses or not had been opened for a long time until 1998, the discovery of the neutrino oscillation by Super-Kamiokande experiment[2].

2.2 The target of our R&D

2.2.1 Next generation water Cherenkov detectors

In the last few decades, underground water Cherenkov detector experiments, such as Super-Kamiokande, have been extremely successful in achieving the new physics results, including confirmation of solar neutrino flux deficit[3, 4], evidence for atmospheric neutrino oscillation[2] and its oscillatory signature[12], evidence for mu-neutrino disappearance using accelerator-generated neutrinos[13], and setting the world best limit on the nucleon decay[14, 15, 16].

The water Cherenkov detector consists of a large water tank and photosensors surrounding the tank. When a charged particle moves faster than the speed of the light in water, it generates the Cherenkov light. Since all the generated Cherenkov lights have the same angle with respect to the velocity of the particle, the light forms a cone and the hit pattern of the photosensors on the tank walls forms the ring pattern. The timing and the shape of the ring pattern tell us the position and energy-momentum vector of the charged particle. Based on the ring pattern, we can distinguish electrons from muons, since electrons form rather "fuzzy" ring patterns due to electromagnetic cascade shower, while muons don't.

The merits of the water Cherenkov detector are its large interaction volume and its hermeticity. The large interaction volume is suitable for the detection of very rare events, such as neutrino interaction or proton decay. The hermeticity reduces the possibility to miss signals from a particle, and thereby enhances the efficiency of the event identification. The high efficiency is useful in various analyses, e.g., it highly suppresses backgrounds from misidentifications in the rare decay search.

To reach better physics sensitivity, several "next generation" water Cherenkov detector experiments with a larger volume detector are proposed. One example is Hyper-Kamiokande project in Japan[17]. The volume of the detector is about one megaton, which is 20 times larger than that of Super-Kamiokande (Fig. 2.1).

Assuming the same coverage of photosensors as Super-Kamiokande, we need a quite large number (about 200,000) of photosensors. If we use the 20-inch PMTs that are used in Super-Kamiokande, total cost of the experiment might be prohibitive. To realize such a huge experiment, cost reduction of photosensors is necessary. Needless to say, upgrades in performance of photosensors are also awaited.

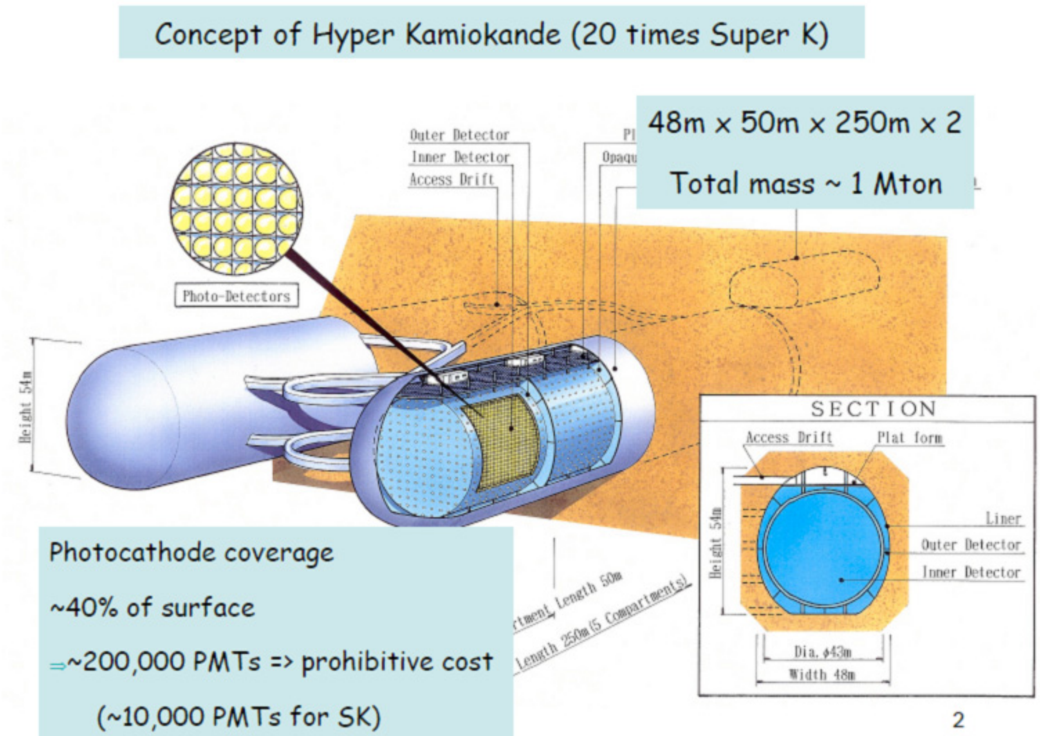

Figure 2.1: A schematic drawing of proposed Hyper-Kamiokande experiment.

2.2.2 Requirements to photosensors in next generation water Cherenkov detectors

Major requirements to the photosensors in next generation water Cherenkov detector experiments are

1. simple structure,
2. time resolution better than $\sigma = 1\,\mathrm{ns}$,
3. single photon sensitivity,

4. a large sensitive area, and

5. a wide dynamic range up to ∼300 photoelectrons.

The first one is essential for cost reduction on mass production. The second one is required for the better position resolution of vertex reconstruction[a]. The third and forth ones are important for the ring pattern recognition. The last one enables us to detect high energy cosmic neutrinos.

Our solution to these requirements is to employ an Hybrid Avalanche Photo-Detector (HAPD) with a large photocathode. HAPD is a new photosensor under development, based on an unique idea of combining vacuum tubes and silicon device technology. It has a very simple structure with no dynodes, a good timing response, capability to detect single photon, a large sensitive area, and a wide dynamic range. These characteristics exactly suits the requirements listed above, and hence we have developed HAPDs as photosensors in the next generation water Cherenkov detectors.

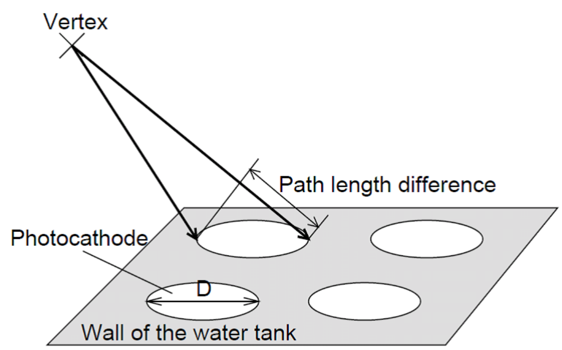

Figure 2.2: The picture shows the path length difference between two Cherenkov photons originated from the same vertex and reaching the same photosensor.

2.3 What is HAPD?

2.3.1 History of HPD and HAPD

In this section, we briefly describe an Hybrid Avalanche Photo-Detector (HAPD).

[a]Position resolution of the vertex reconstruction is dependent on the time resolution of the photosensors. With photosensor with better time resolution, we can achieve better position resolution of the vertex reconstruction. However, there is another dilution effect due to the fact that we cannot determine where the incident photon hits in the photosensitive area of the photosensor. The path length difference is of the order of D, the diameter of the photosensor's sensitive area (See Fig. 2.2). Therefore, the dispersion of the photon arrival timing on the photosensor is D/c', where c' is the speed of the light in water. Since we use the photosensors whose D is ∼30 cm, D/c' is ∼1.5 ns. Time resolution of the photosensors should be equal or better than D/c'. We set the requirement to be 1 ns.

An Hybrid Photo-Detector (HPD), combination of a photocathode and a silicon device, was proposed by F. A. White and J. C. Sheffield in 1962[18]. HPDs are introduced to the particle physics experiments by R. Desalvo in 1987[19]. As HPDs have been improved rapidly and have achieved the quality of practical use[20], some major experiments are planning to use HPDs as photosensors[21, 22, 23, 24].

An Hybrid Avalanche Photo-Detector (HAPD) is an HPD equipped with an avalanche diode (AD)[b]. Since HAPD has one or two orders of magnitude larger gain than HPD thanks to the additional gain by the avalanche effect, it has a great advantage in detecting a single photon. , although AD is relatively difficult to control than usual Silicon devices. Therefore, it has been studied intensively as a candidate to replace the PMT.

In 1997, M. Suyama *et al.* reported on a practical HAPD[27]. N. Kanaya *et al.* made its detailed evaluation[28]. The HAPD has been developed successfully, and it is now commercially available[29]. HAPD attracts, now, much attention in various fields such as gamma-ray telescopes[30, 31], time-of-propagation (TOP) counters[32, 33], and a detector for future linear colliders[34].

Based upon the background described above, we started to develop an HAPD with a large photocathode as photosensors for next generation water Cherenkov detectors. By 2002, we developed a 5-inch prototype HAPD and A. Kusaka made its evaluation[35].

An HPD with a multi-pixel AD, which has position resolution, has also been developed recently [37, 38].

Note that HPD/HAPD is also called an "electron bombardment sensor (EB sensor)".

2.3.2 The principle of HAPD

The working principle of an HAPD is as follows. Photons are converted into photoelectrons at the photocathode and then accelerated by the HV applied between the photocathode and the AD. When an electron is driven to the depletion region of the reverse biased P-N junction of the AD, it creates electron-hole pairs. This multiplication process is called "bombardment gain." If the energy of the incident electron is low enough so that it stops in the AD, the number of the electron-hole pairs is proportional to the energy of the incident electron.

When the AD is reverse-biased, to the extent not to exceed the breakdown voltage, the electron-hole pairs created by an incident electron are further multiplied, due to the avalanche effect. This second multiplication process is called "avalanche gain."

The total charge created in the AD is proportional to the number of incident photoelectrons.

[b]Note that the avalanche diode usually detect photons and is called avalanche photo-diode (APD), although we call it avalanche diode (AD) since in our case it detect electrons, not photons.

2.3.3 Comparison of HAPD and PMT

Table 2.3 summarizes the comparison of major performances of HAPD and PMT[39, 40, 41]. Pros and cons of HAPD are listed as follows.

Pros:

- HAPD has fair possibility to be low cost, since it has no dynodes and hence has much simpler structure.
- HAPD has better timing characteristics than PMT, since it has no dynodes and the trajectory length is almost same for all photoelectrons.
- The statistical gain fluctuation of HAPD is so small that very clean photon counting is possible, since it has high gain (typically more than 1000) in the first multiplication stage ("bombardment gain") [c].

Cons:

- We need to develop a dedicated low-noise readout system, since the total gain of the HAPD is about two order smaller than that of PMT.
- HAPD demands much higher voltage and we need to treat the insulation carefully.

In our R&D, evaluation of basic characteristics of HAPD and development of low-noise readout system are important. The evaluation is discussed in Chapter 3 and the development of the dedicated readout system is discussed in Chapter 4.

[c] The total gain G of multi-stage multiplication is given by

$$G = \delta_1 \delta_2 \cdots \delta_n. \tag{2.9}$$

In case of PMT, n$\sim$10 and $\sigma_i \sim 10$. In case of HAPD, n=2, $\sigma_1 =\sim 4500$ (bombardment gain, when HV=20 kV) and $\sigma_1 =\sim 30$ (avalanche gain). The output fluctuation for the 1 photoelectron input is given by

$$\frac{\Delta G}{G} = \sqrt{\frac{1}{\delta_1} + \frac{1}{\delta_1 \cdot \delta_2} + \cdots + \frac{1}{\delta_1 \cdots \delta_n}}, \tag{2.10}$$

and the fluctuation of the total gain are dominated by the gain fluctuation of the first multiplication stage (See [42]).

	13-inch HPD	13-inch PMT (R8055)	20-inch PMT (used in Super-K)
Number of structure units	$\sim$300	$\sim$3000	$\sim$3000
Time resolution (ns)	0.3 (simulation, at 20kV)	1.2	2.3
Rise time (ns)	0.9	6	10
Pulse width (ns)	3	10	20
Gain	$\sim 10^5$	$\sim 10^7$	$\sim 10^7$
Operating voltage	20 kV	1.5 kV	2 kV

Table 2.3: Comparison of HAPDs and PMTs.

Chapter 3

R&D of HAPD

A 5-inch prototype HAPD was tested before. We have developed a 13-inch HAPD. In this chapter, we discuss the performance of the 13-inch HAPD and consider whether it satisfies the requirements for the next generation water Cherenkov detectors.

3.1 R&D of 5-inch HAPD

Prior to this thesis, a 5-inch prototype HAPD had been developed. The outcome of these development was reported in detail by A. Kusaka[35]. Here are some major results.

Operating HV	Gain	Time resolution	S/N ratio
-8.5 kV	4.4×10^4	0.4 ns	21

Table 3.1: The performance of 5-inch prototype HAPD. These time resolution and S/N ratio are obtained applying the digital filter.

3.2 Specifications of 13-inch HAPD

We have developed an HAPD with a 13-inch diameter photocathode. Fig. 3.1 is a picture of our HAPD. Its structure is shown in Fig. 3.2.

The size of the photocathode (effective area) is 332 mm (240 mm) in diameter. The applied HV between the photocathode and the AD is designed to be 20 kV, corresponding to ~ 4500 electron-hole pairs in the first multiplication stage ("bombardment gain"). However, we have a problem in the insulation of the HV. In this thesis we show the data taken with the HV of 12 kV or 15 kV. The applied reverse bias voltage on the AD is ~ 370 V, chosen to achieve maximum gain with a tolerable AD leak current. Size of the AD is 5 mm in diameter. The AD is epitaxial[43, 44], front-side illumination type. Our HAPD works on positive HV mode, i.e. the photocathode is connected to ground and the AD is on the positive HV[a]. The AD is AC-coupled to the readout electronics with two 140 pF capacitors (See Fig. 3.3). Note that because we focus mainly on confirming the fundamental performance of the prototype, the electron trajectories have not been optimized and the effective area of the photocathode is smaller compared to the physical diameter of the HAPD. Note that we are planning to upgrade the tube structure and achieve an effective area of 300 mm in diameter (See Section 3.3.9).

Figure 3.1: The picture of the 13-inch HAPD.

Photocathode diameter	332 mm (13 inch)
Photocathode effective diameter	240 mm
Photocathode material	Bialkali
AD Size (diameter)	5mm
AD type	Front-side illumination type
AD capacitance	~ 70 pF at bias voltage of ~ 370 V

Table 3.2: Basic characteristics of a 13-inch HAPD.

[a]Because our HAPDs are to be used in a water tank of the water Cherenkov detector, the photocathode must be grounded.

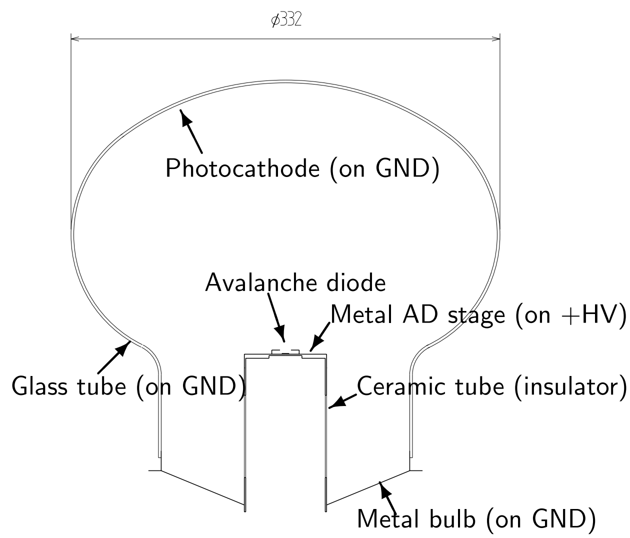

Figure 3.2: The structure of the 13-inch HAPD.

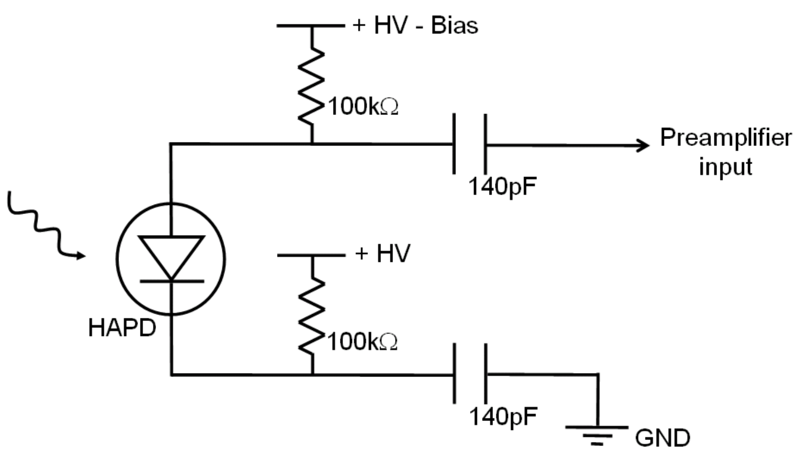

Figure 3.3: The AD is AC-coupled to the readout system.

3.3 Performance evaluation of 13-inch HAPD

Fig. 3.4 schematically shows the setup for the HAPD performance evaluation.

A raw signal from the HAPD is amplified by a wide bandwidth [b] preamplifier. The waveform of the amplified signal is sampled and digitized by an oscilloscope[c] and stored on a hard disk. Note that we use an oscilloscope only for the HAPD performance evaluation. In the future experiment, we plan to use a waveform sampler such as FADC and/or AMC. After the waveform sampling, we apply the digital filtering algorithm to the data stored in the oscilloscope, in order to achieve better S/N ratio and time resolution. As a light source, we use Picosecond Light Pulser (PLP)[d] with $\lambda = 441\,\mathrm{nm}$, attached to the photocathode with an optical fiber cable. The Earth's magnetic field is shielded to be $< 0.2\,\mathrm{Gauss}$ inside the light shielding box.

3.3.1 Raw signal

Fig. 3.5 shows a raw signal of the HAPD with the applied HV of 12kV. The rise time is ∼1 ns and the pulse width is ∼6 ns. The HAPD shows a good timing response.

3.3.2 Avalanche gain and bombardment gain

We measure two kind of gain characteristics, the bombardment gain and the avalanche gain. The measurement is performed in a "current mode," that is, we measure the ratio of the current which flows the AD (See Fig. 3.6) as a function of HV or AD bias voltage. To subtract background due to the AD dark current, we measure the difference of the currents with and without the light input.

Fig. 3.7 shows the bombardment gain as a function of the applied HV. We vary the HV from 0 kV to 12 kV, with the AD bias voltage fixed to be 50 V, in order to disable the avalanche gain. The gain curve rises at HV of ∼3 kV, because there is a nonsensitive layer on the depletion layer of the AD and the incident electron loses some energy in the nonsensitive layer (See [26]). The slope of the gain curve is ∼ 1/3.6V, which corresponds to the creation energy of an electron-hole pair in Silicon. The bombardment gain is ∼2400 at the HV of 12 kV.

Fig. 3.8 shows the avalanche gain as a function of the AD bias voltage. We vary the AD bias voltage from 0 V to 368 V, with the HV fixed to be 12 kV. The gain is normalized to be 1 at the bias voltage of 40 V, since avalanche effect take place at $\geq 40\,\mathrm{V}$. The avalanche gain is ∼20 at the maximum AD bias voltage of 368 V.

In total, we achieve the gain of ∼50,000.

---

[b] Preamplifier bandwidth is designed to be as wide as possible. High frequency region where noise component dominates is suppressed afterwards by digital filtering.

[c] Infinium 54825A, by Hewlett Packard. Its bandwidth is 500 MHz and its sampling rate is 2 GHz.

[d] PLP-02, by Hamamatsu Photonics. Its pulse width is less than 50 ps. Its trigger jitter is less than 10 ps.

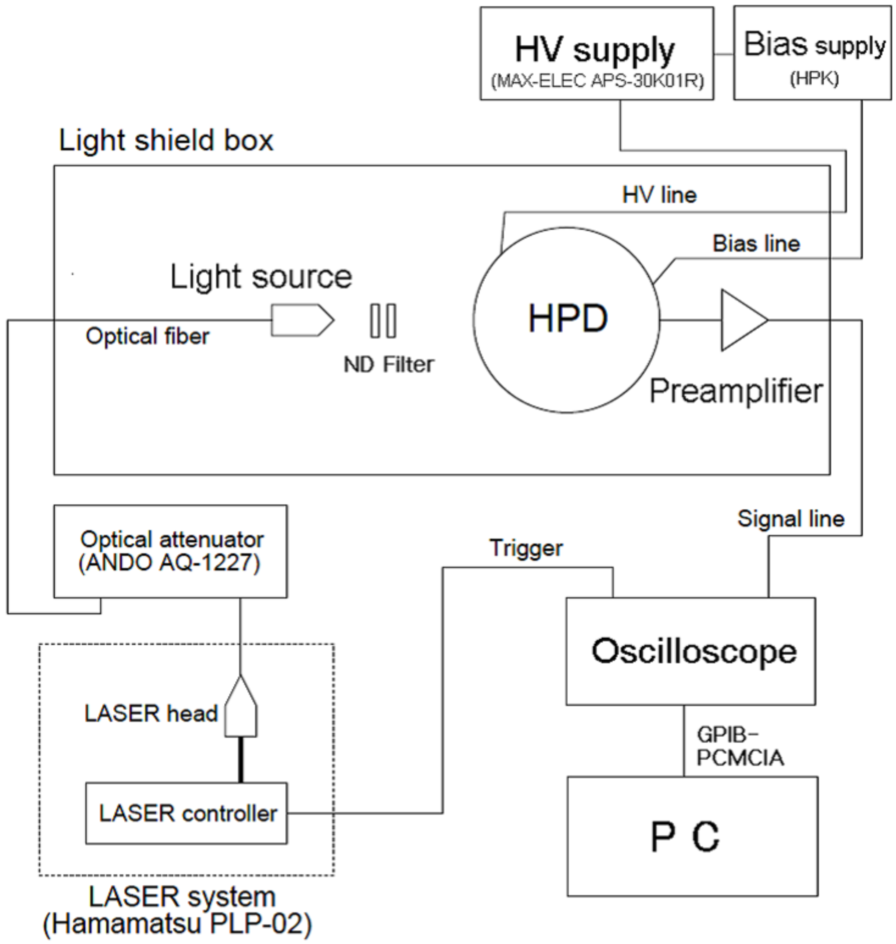

Figure 3.4: The measurement setup for the HAPD performance evaluation.

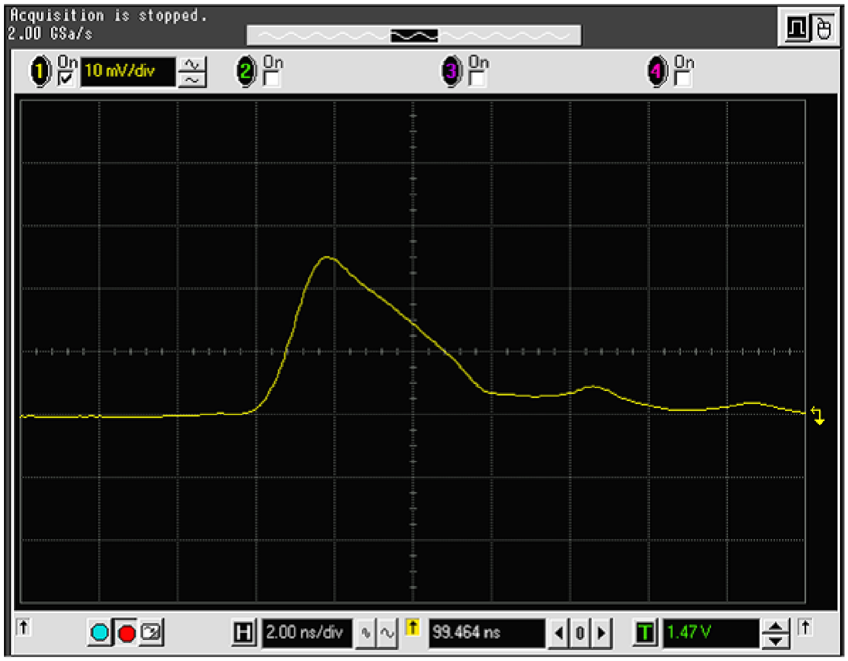

Figure 3.5: The raw signal of the HAPD on acceleration voltage of 12 kV. The light input is equivalent to ∼30p.e. The horizontal scale is 2 ns/div and the vertical scale is 10 mV/div.

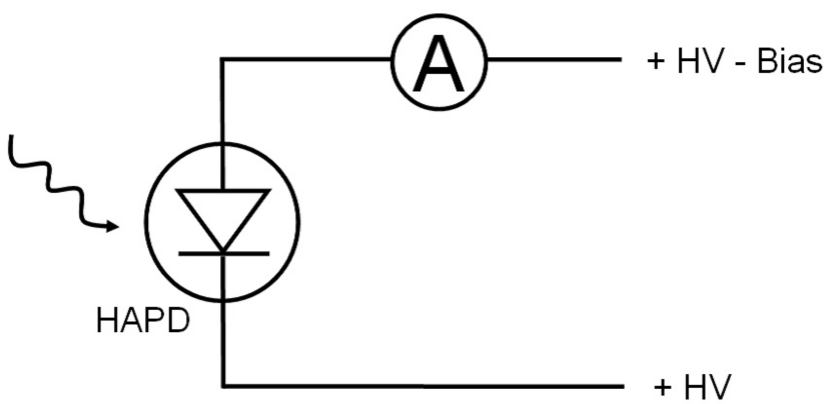

Figure 3.6: The measurement setup of the "current mode."

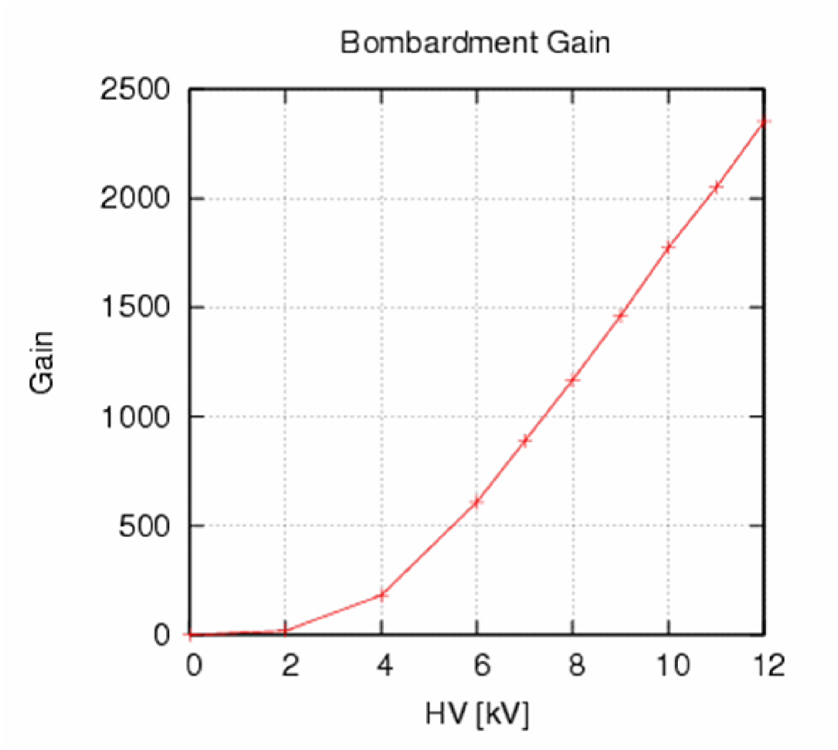

Figure 3.7: The bombardment gain as a function of the applied HV.

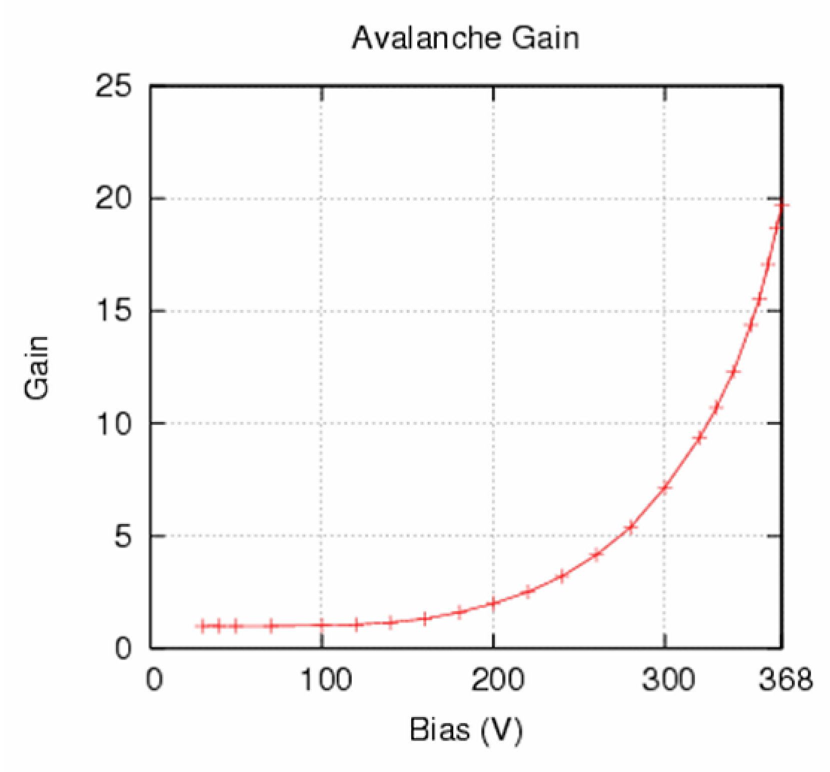

Figure 3.8: The avalanche gain as a function of the AD bias voltage.

3.3.3 Pulse height spectrum

Fig. 3.9 shows a pulse-height histogram after application of the digital filter. The applied HV is 12 kV and the AD bias voltage is 368V. The horizontal axis is calibrated using a test pulse input charge. By fitting each peaks with Gaussian functions, $\sum_{i=0}^{n} C_i \exp(-(x-\mu_i)/(2\sigma_i^2))$, we obtain the peak position of each peak, μ_i. We define the detector gain as the slope of the linear fit of μ_i as a function of the number of photoelectron i. The detector gain is 24,000[e]. The S/N ratio for 1 p.e. signal is given by μ_1/σ_0. The S/N ratio is 10. The equivalent noise charge (ENC) is given by σ_0. The ENC is 2,400. We can observe clear photon counting up to ~ 5 photoelectrons (p.e.).

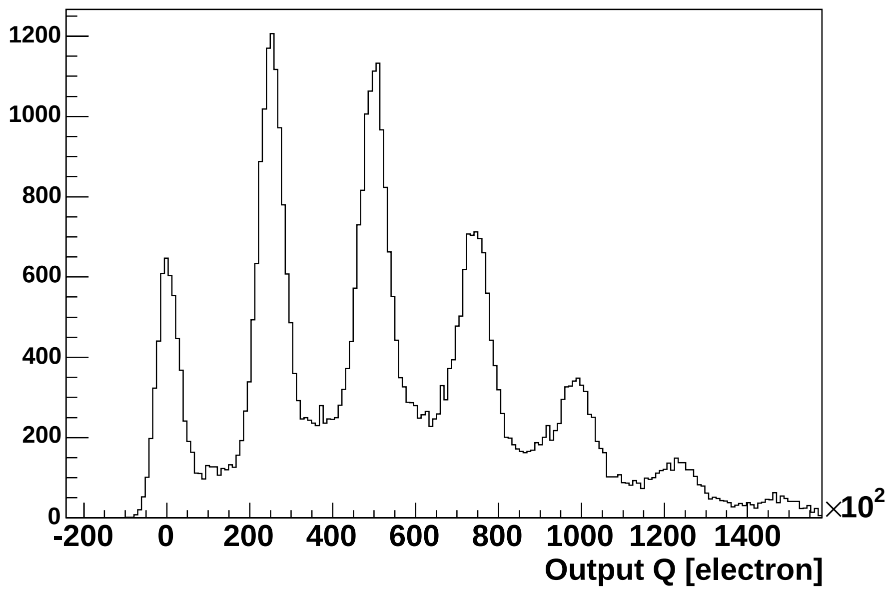

Figure 3.9: The pulse-height histogram after the application of the digital filter (section 4.4).

3.3.4 Time resolution

Fig. 3.10 shows the peaking time distribution of 1p.e. equivalent signals. We define the time resolution as a sigma of the Gaussian function fitted to the histogram of the peak timing of the output signal. Fig. 3.11 shows time resolution vs. number of input photoelectrons. The time resolution is $\sigma \sim 0.7$ ns for 1 p.e. signal, and better for ≥ 2 p.e. signals. Note that this time resolution includes not only time

[e]This gain is smaller than the product of the bombardment gain and the avalanche gain. This is because not all the charge generated by the detector flows into the readout system (See Fig. 4.2.1).

resolution of the HAPD itself, but also that of the readout system. Thanks to the absence of dynodes, time resolution of the HAPD is significantly better than that of 20-inch PMTs used in Super-Kamiokande[f].

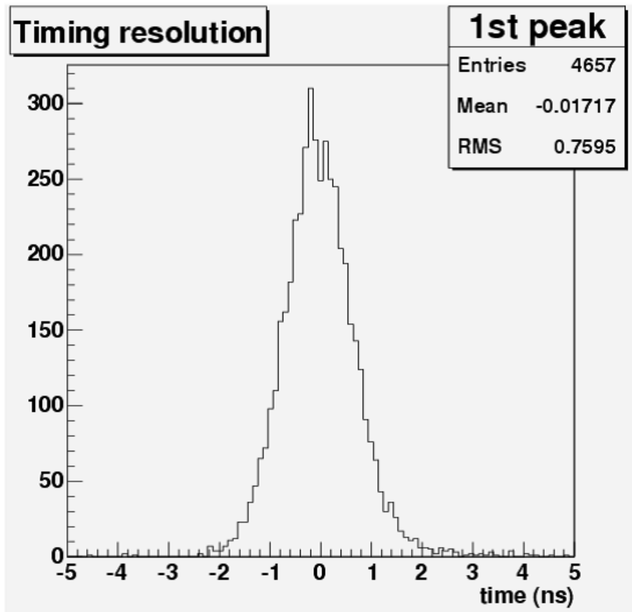

Figure 3.10: The peaking time distribution of 1.p.e. equivalent signals after the application of the digital filter (section 4.4).

3.3.5 Pulse-height spectrum and time resolution of 13-inch PMT

We measured the pulse-height spectrum and time resolution of the 13-inch PMT (R8055) by the same method which is applied to the 13inch HAPD, except that we use no preamplifier in this case. Operated at 1.78 kV of HV, the 13-inch PMT shows the gain of $\sim 10^7$ and the time resolution of $\sigma \sim 0.7\,\mathrm{ns}$ for 1.p.e. equivalent signal (See Fig. 3.12 and Fig. 3.13).

3.3.6 Linearity

Fig. 3.14 shows the output pulse height as a function of the number of the input photoelectrons. Linearity was measured by varying the input light intensity by changing the ND filters[g]. The dominant source of the error bars in Fig. 3.14 are the

[f] Time resolution of the 20-inch PMTs used in Super-Kamiokande is $\sigma \sim 2.2\,\mathrm{ns}$ for 1 p.e. signal (see [41]).

[g] Manufactured by Sigma Koki Co., Ltd.
http://www.sigma-koki.com/

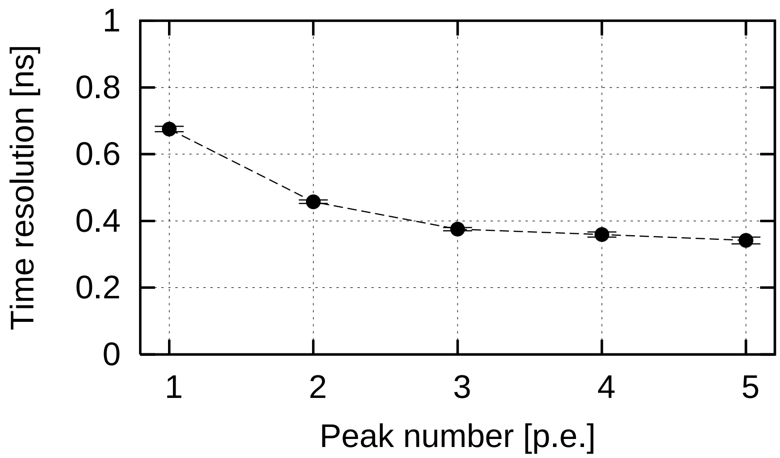

Figure 3.11: The time resolution as a function of the number of input photoelectrons after the application of the digital filter (section 4.4).

tolerance of the transmittance of the ND filters. Linearity holds up to ∼150p.e., which is limited by the saturation of the preamplifier.

3.3.7 Gain and transit time uniformity over the photocathode

Uniformity is measured by changing the position of light source, attached onto the photocathode. We move the light source in only one direction over the photocathode.

Fig. 3.15 shows the gain uniformity over the photocathode. We set the input light intensity to be ~ 2 p.e. equivalent on average. For the gain value, we use the slope of the linear fit of the peak position in Fig. 3.9 as a function of corresponding number of photoelectrons. Each error bar represents the error of the linear fit(See Section 3.3.3).

Fig. 3.16 shows the transit time uniformity over the photocathode. We set the input light intensity to be ~ 30 p.e. equivalent on average. Each error bar represents the time resolution at each position of the light source.

3.3.8 Dark count rate

Fig. 3.17 shows the pulse-height spectrum after the application of the digital filter, with no light input. Measurement is performed after putting the HAPD in the light shielding box for two hours with no light input. Applied HV is 15 kV, the temperature is 15°C. Counting the signals with the amplitude larger than 0.75 p.e. equivalent, we observe the dark count rate of ∼100kHz, which is much worse

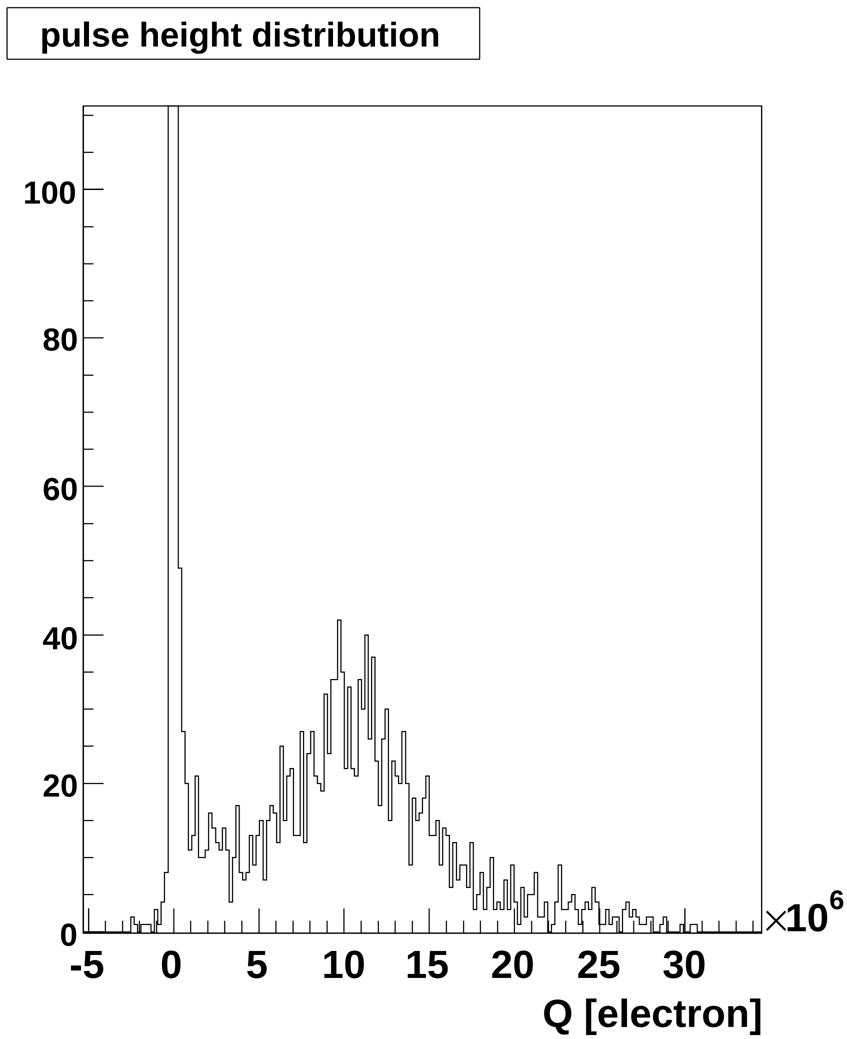

Figure 3.12: The pulse-height spectrum of the 13-inch PMT, after the application of the digital filter (section 4.4), operated at HV=1.78kV. We use no preamplifier.

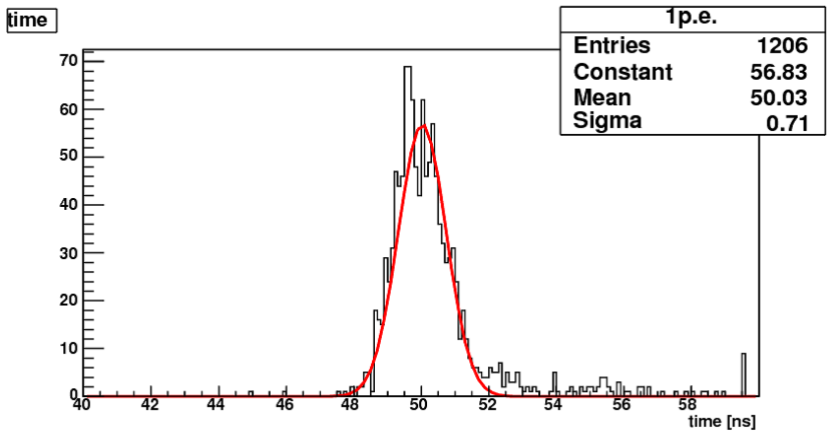

Figure 3.13: The peaking time distribution of 1.p.e. equivalent signals of 13-inch PMT, after the application of the digital filter (section 4.4), operated at HV=1.78kV. We use no preamplifier.

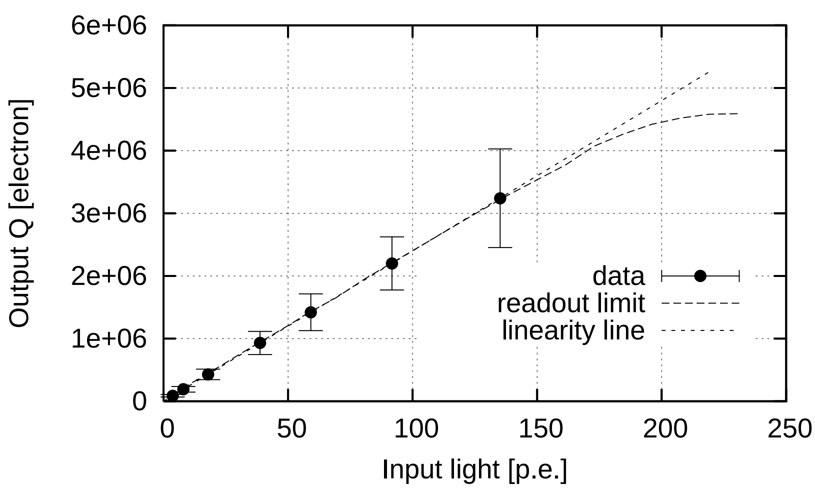

Figure 3.14: The output pulse height as a function of the number of the input photoelectrons, with a measured linearity curve of the preamplifier.

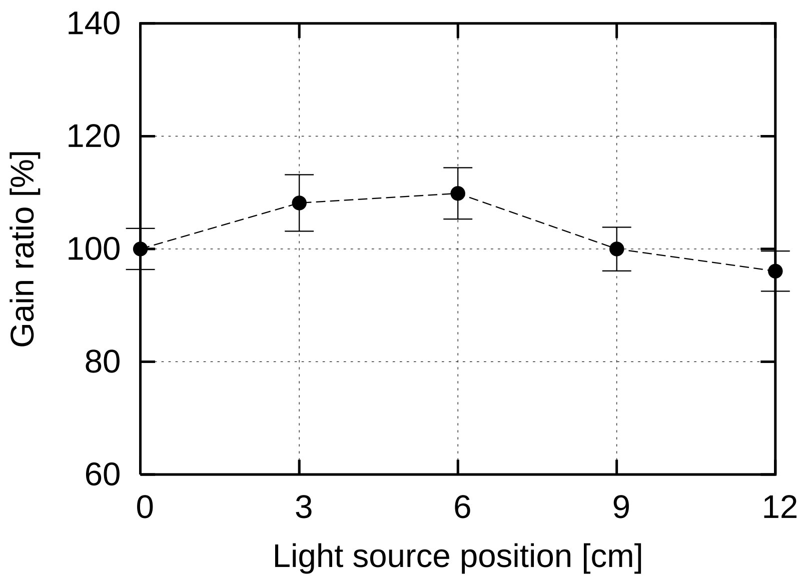

Figure 3.15: The gain uniformity over the photocathode. The horizontal axis is the light source position from the center of the photocathode.

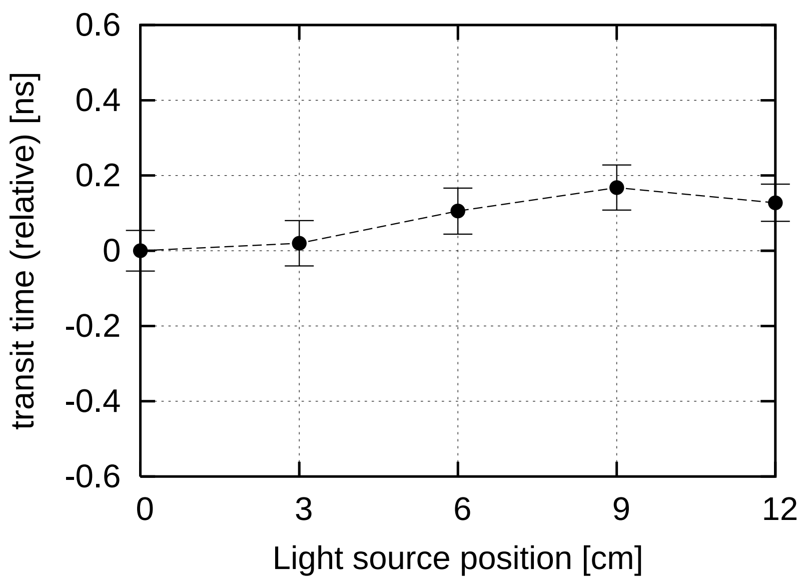

Figure 3.16: The transit time uniformity over the photocathode. The horizontal axis is the light source position from the center of the photocathode.

compared to that of 20-inch PMTs used in Super-K[h]. We consider the reason is as follows. The dominant source of the dark count of the large HAPD is thermal electron emission from the photocathode, and the thermal electron emission rate is much dependent on the fabrication process of the photocathode. However, we have not optimized the process yet and we consider this is the reason for the worse dark rate. The supporting fact is that we observe larger photocathode sensitivity than expected, in long wavelength region (cathode lumen sensitivity, S_k, is $98\,\mu$A/Lm and cathode lumen sensitivity for blue, S_{kb}, is $7.7\,\mu$A/Lm-b).

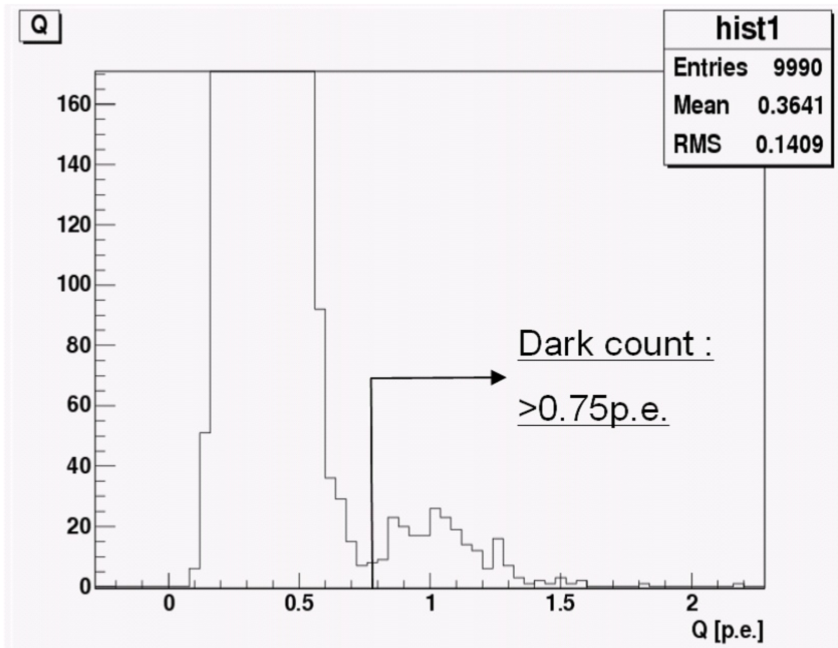

Figure 3.17: The pulse-height spectrum after the application of the digital filter (section 4.4), with no light input, operated at HV=15 kV.

3.3.9 Upcoming R&D issues of 13-inch HAPD

- Tube structure R&D

  We are developing new tube structure, which has larger sensitive area (240 mm → 300 mm), and better resistance to the water pressure (2.5 atm → 7.5 atm). To improve the insulation performance, we are also trying to replace the ceramic insulation tube with the glass one.

- Decoupling capacitor R&D (larger capacitance)

[h] 20-inch PMTs used in Super-K have a dark count rate of ∼10 kHz at a temperature of 10°C, where the dark count rate is defined by the rate of pulses greater than 1/4 p.e. in magnitude [41]. The detailed discussion is in Appendix A

We are developing new decoupling capacitors, which have larger capacitance (140pF $\rightarrow$ 4000pF). With larger decoupling capacitances, more charge generated by the detector flows into the readout (See Section 4.2.1).

- New type of AD (back-side illumination type)

  We are developing new ADs called "back-side illumination type AD." Fig. 3.18 schematically shows the structure of the front-side illumination AD and the back-side illumination AD. The back-side illumination AD is considered to have smaller detector capacitance ($\sim$30pF) and superior performance in terms of surface damage caused by electron bombardment. It is also considered to be more robust to the alkali pollution when we activate the photocathode.

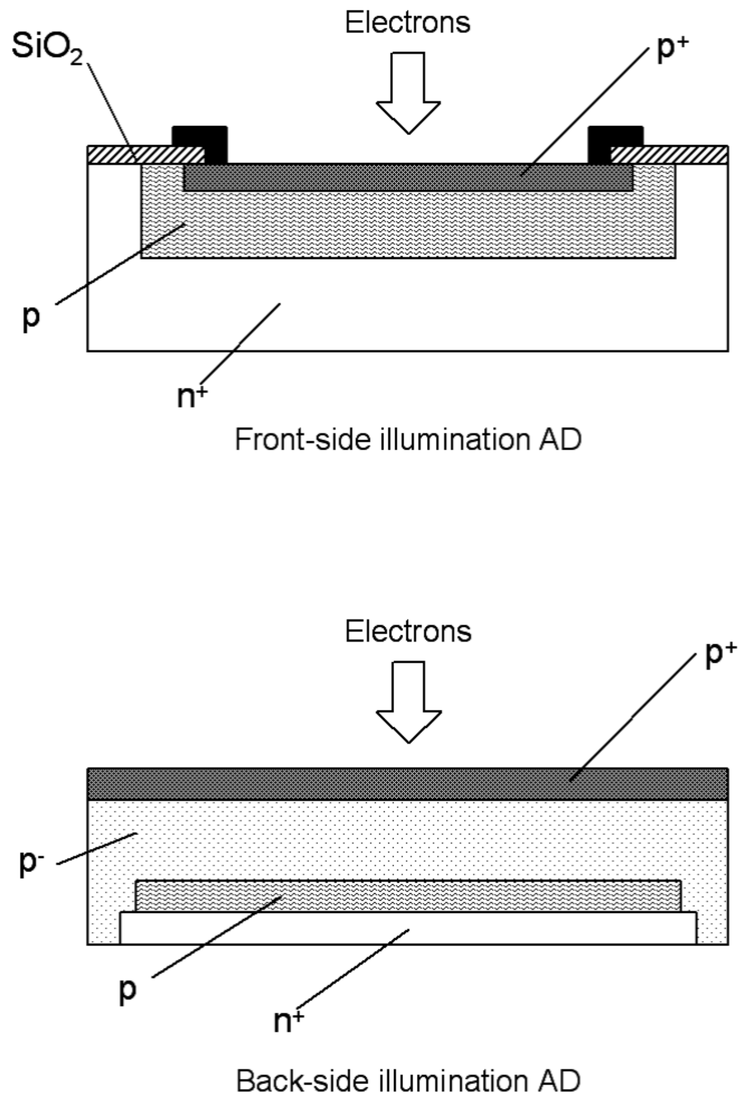

Figure 3.18: The upper (lower) figure shows the the structure of the front-side (back-side) illumination AD.

Chapter 4

R&D of readout system

A dedicated low-noise readout system for our HAPD must be developed in order to achieve HAPD's excellent performances discussed in the previous chapter. In this chapter, we discuss the R&D of the readout system. We developed a novel readout system for 13-inch HAPD.

In Section 4.1, we describe the design concept of our readout system. In Section 4.2, we describe R&D of a prototype discrete circuit preamplifier and an ASIC preamplifier. In Section 4.3, we describe R&D of an AMC ASIC prototype as a waveform sampler. In Section 4.4, we describe R&D of digital filtering algorithm and its implementation on FPGA.

4.1 Design concept of readout system

Requirements to the readout system are as follows:

Low noise In order to detect a single photon, with HAPD whose gain is $\sim 10^5$, one or two orders of magnitude smaller than that of PMT, the noise level of the readout system must be low enough. Low noise is also essential for good time resolution.

Good time resolution better than 1ns Since the time resolution of the whole system is determined by that of HAPD itself (i.e. dispersion of the photoelectron trajectory length) and that of the readout system, the readout system must have time resolution better than 1ns, which is required for the whole system.

High yield and low cost on mass production In next generation water Cherenkov detector experiments, a quite large number (∼200,000) of sensors are needed. Therefore high yield and low cost on mass production are of serious interest. ASIC preamplifier and AMC ASIC have advantage over other devices in this regard.

Fig. 4.1 schematically shows our readout system. It consists of 1) a fast (wide bandwidth) and low-noise preamplifier, 2) a high speed (∼1 GHz) waveform sampler, and 3) a digital filter to extract signal amplitude and timing information.

Note that we feed the output signal from the preamplifier directly into a waveform sampler, without any shaping amplifier, because digital filtering algorithm after the waveform sampler plays the role of the shaping amplifier.

The uniqueness of our system is that we are not using a traditional shaper+ADC+TDC solution. Instead, we adopt a waveform sampler and a digital filter, because the performance of digital filters is much superior to that of analog shapers and we can highly enhance the S/N ratio and time resolution. We can adopt digital filters only when we use a waveform sampler, not ADC+TDC.

4.2 Preamplifier

Firstly we describe the requirements to preamplifier. Secondly we report the R&D of our discrete circuit preamplifier. Finally we report the R&D of our ASIC preamplifier, version "ASIC2004." Picture of the preamplifiers are shown in Fig. 4.2.

Preamplifiers described in this chapter have been developed and evaluated by Y. Kawai (HPK).

4.2.1 Requirements

Requirements to the preamplifier are 1) wide bandwidth, 2) large input capacitance, 3) low noise, and 4) wide dynamic range.

1. Bandwidth of the preamplifier must be as wide as possible. Even though wider bandwidth results in more noise rather than more signal, we can achieve larger S/N ratio and better time resolution with wider bandwidth because noise component can be suppressed afterward by digital filter algorithm. Wide bandwidth is equivalent to the fast rise time of the preamplifier output signal.

2. Large input capacitance, or low input impedance, is essential to achieve larger gain, because the charge which flows into preamplifier, Q, is given by the following equation (see Fig. 4.3):

$$Q = Q_{total} \cdot \frac{C'}{C_{det} + C'} \quad \left(C' \equiv \frac{(C_{decouple}/2) \cdot C_{in}}{(C_{decouple}/2) + C_{in}} \right), \tag{4.1}$$

   where Q_{total} is the total charge generated by the detector, $C_{decouple}$ is the capacitance of the decoupling capacitor, and C_{in} is the input capacitance of the preamplifier[a]. Large input capacitance C_{in} can be achieved by large open

[a] $C_{decouple}$ is 140 pF. Typical detector capacitance is 70 pF. With larger C_{in}, we lose less signal charge. However, even if we can achieved the $C_{in} = \infty$, $Q = 0.5 \cdot Q_{total}$ and we lose 50% of the signal. To overcome this problem, smaller detector capacitance and larger decoupling capacitance are essential. We are planning to upgrade our AD and decoupling capacitors, and will achieve

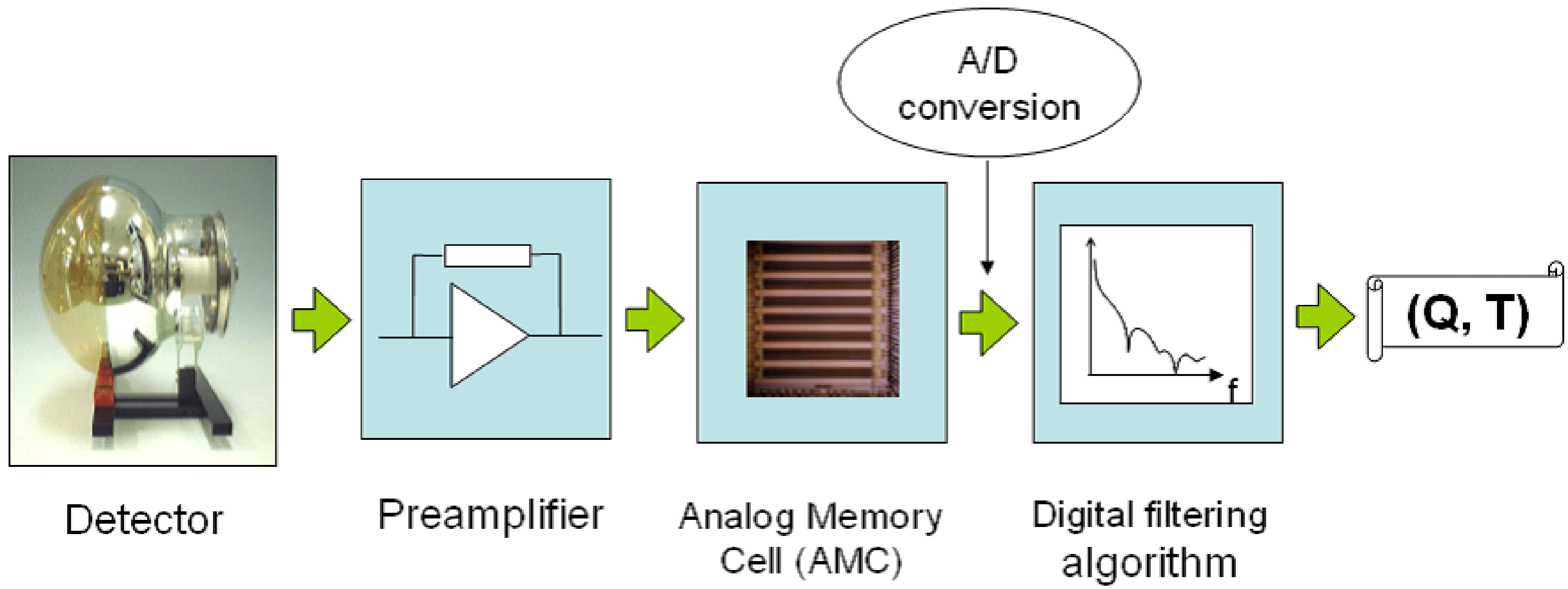

Figure 4.1: Our readout system consists of 1) a fast and low-noise preamplifier, 2) a high speed ($\sim$1 GHz) waveform sampler (Analog Memory Cell), and 3) a digital filter to extract signal amplitude and timing information. More realistic readout system in a water Cherenkov detector is described in Appendix B.

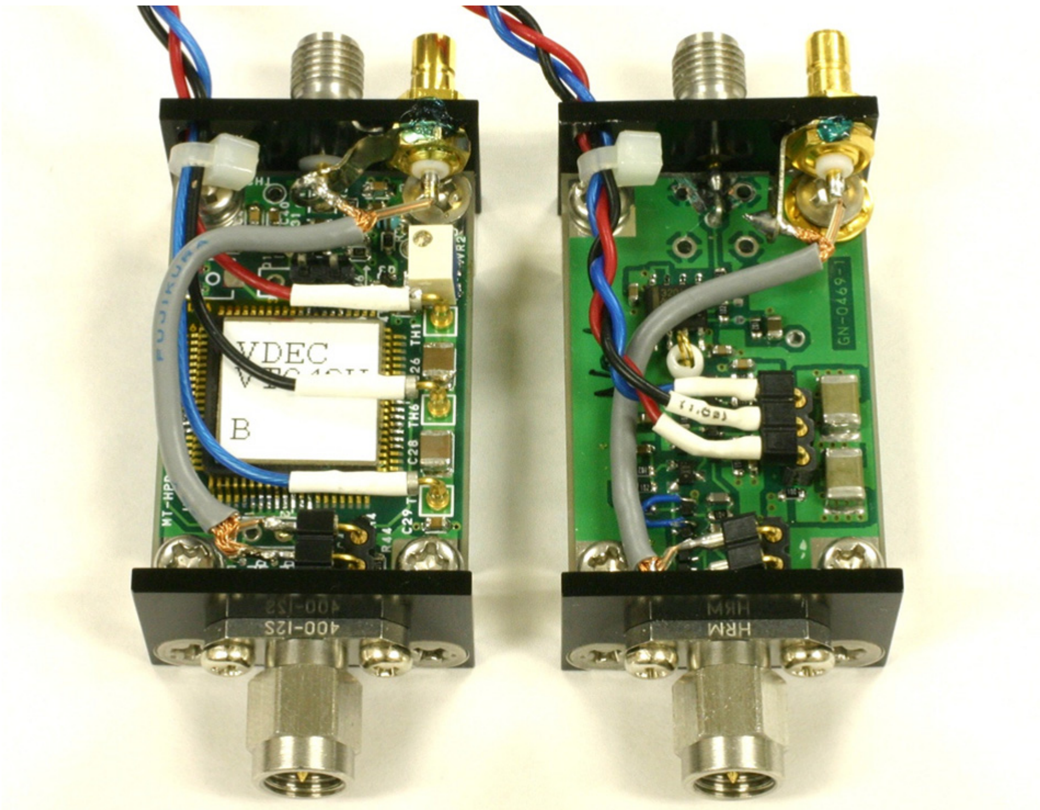

Figure 4.2: The picture of the discrete circuit preamplifier (left) and the ASIC preamplifier version "ASIC2004" (right).

loop gain, since C_{in} is given by $C_{in} = C_f \times (A + 1)$, where C_f is feedback capacitance and A is the open loop gain.

3. Since the gain of the HAPD is $\sim 10^5$, the ENC of the preamplifier must be well below 10^5 electrons, in order to detect single photon. Here we demand ENC to be less than $\sim 10^4$ electrons.

4. In order to meet the dynamic range requirement of the readout system (300 p.e.), preamplifier must have dynamic range of more than 300 p.e.

We need to develop the preamplifier which meets the requirements listed above.

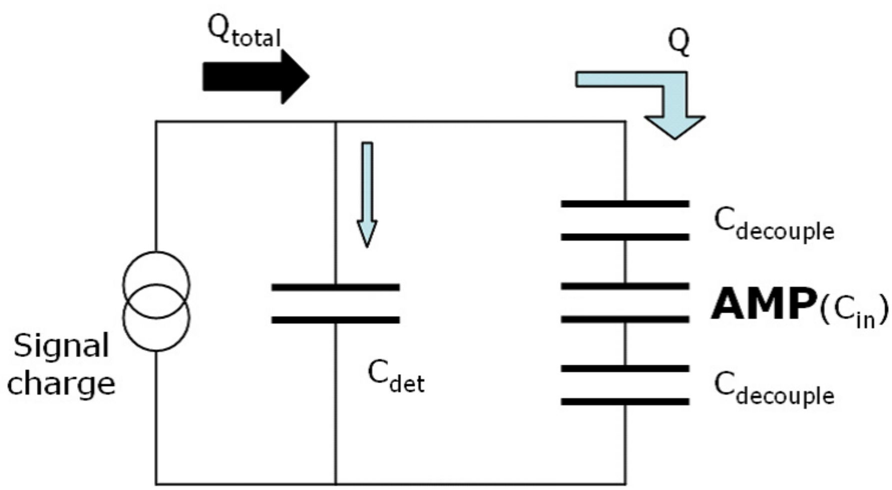

Figure 4.3: The equivalent circuit of the HAPD connected with the preamplifier. Q_{total} is the charge generated by detector, $C_{decouple}$ is the capacitance of the decoupling capacitor, and C_{in} is the input capacitance of the preamplifier.

4.2.2 Design concept

We design our preamplifiers following the one developed for the Belle CSI calorimeter[45].

Main ideas are 1) folded cascode charge amplifier with negative feedback, and 2) low noise and fast bipolar transistor as an input transistor and use of several transistors in parallel.

1) The cascode configuration has two merits. First, it increases output impedance. With high output impedance, we can achieve high open loop gain by connecting the

$C_{det} = 30\,\text{pF}$ and $C_{decouple} = 4000\,\text{pF}$ (See Section 3.3.9). Then we lose only 1% of the signal charge if $C_{in} = \infty$.

output to a high impedance node. The high open loop gain is essential to achieve the low input impedance with negative feedback. Second, it reduces unwanted feedback capacitance. It is important to achieve wide bandwidth. There are two type of cascode configuration: "totem pole" configuration and "folded cascode" configuration. They are schematically shown in Fig. 4.4. The merit of the totem pole cascode configuration is that it uses only NPN type transistors and does not need any PNP type transistors, which is slower than NPN type. The demerit is that we need larger power supply voltage to get larger dynamic range, and this results in the larger power dissipation. In addition, we need a level shifter in the signal path as an extra node, and this can be an additional noise source. The merit of the folded cascode configuration is that we need no level shifters. The demerit is we have to use PNP transistors. Considering the merits and demerits, we choose the folded cascode configuration.

2) The input transistor is the most important device, since it is the primary factor which determines the noise performance of the preamplifier. As the input transistor, we use Bipolar Junction Transistor (BJT). The reasons why we select BJT are a)its transconductance, g_m, is large, b) its bandwidth is very wide, and c) its noise performance is good for the wide bandwidth application, compared with other type of transistors. We use several transistors in parallel, in order to reduce the base spreading resistor $r_{bb'}$ of the input transistor, since $r_{bb'}$ is a dominant noise source in high frequency region

4.2.3 Discrete circuit

Fig. 4.5 schematically shows the discrete circuit preamplifier. We use four "2SC5086" transistors in parallel as the input transistor. The voltage supply is +5 V and -5 V. The feedback capacitance is 1pF and the feedback resistance is 100kΩ.

Impulse response

Fig. 4.6 shows the output signals with various capacitors connected in parallel to the preamplifier input, with test pulse input charge of 0.1pC. These capacitors mimic the detector capacitance, hence we call them "pseudo detector capacitance." The rise time[b] of the test pulse input is 5 ns, hence the rise time of the preamplifier itself (t_{rise}^{amp}) is calculated from the rise time of the output signal (t_{rise}) shown in Fig. 4.6 as follows:

$$t_{rise}^{amp} = \sqrt{(t_{rise})^2 - (5\,ns)^2}. \tag{4.2}$$

The result shows two critical features: as a pseudo detector capacitance increases, rise time of the signal becomes slower and output amplitude becomes smaller. Both results indicate that open loop gain of the preamplifier is not large enough. The deterioration of the output signal shape results in a serious problem in deducing the signal amplitude and timing information by digital filters.

[b]The definition of the rise time is 10%-90%.

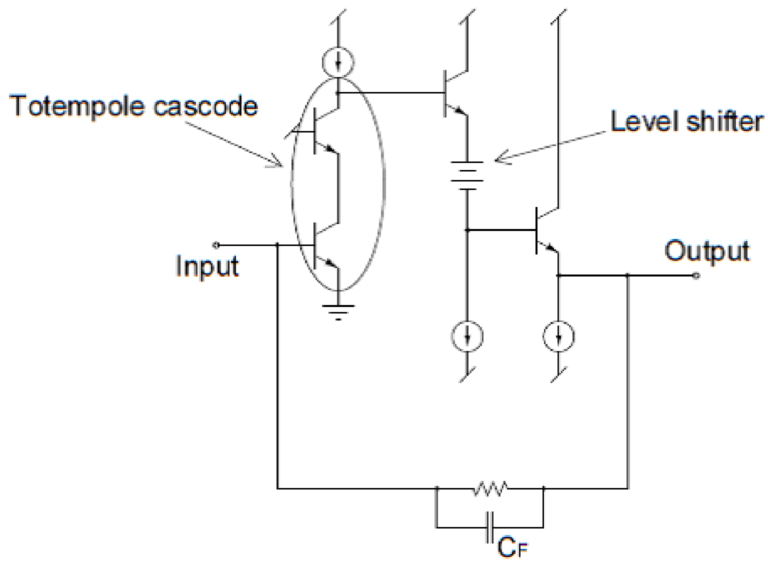

(a) The totem pole cascode configuration.

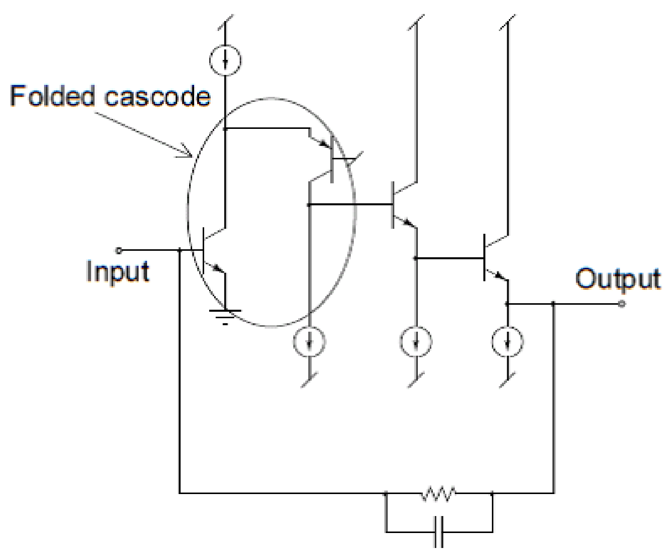

(b) The folded cascode configuration.

Figure 4.4: Two types of the cascode configuration of preamplifier.

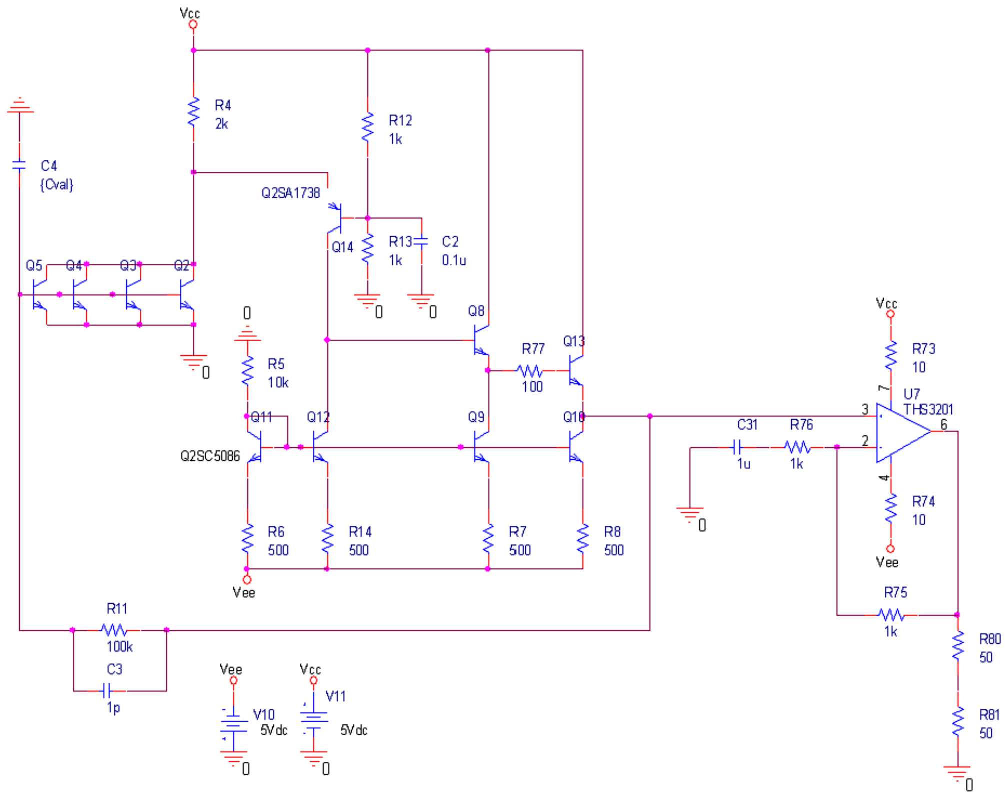

Figure 4.5: The schematic figure of discrete circuit preamplifier. The feedback capacitance is 1pF and the feedback resistance is 100kΩ.

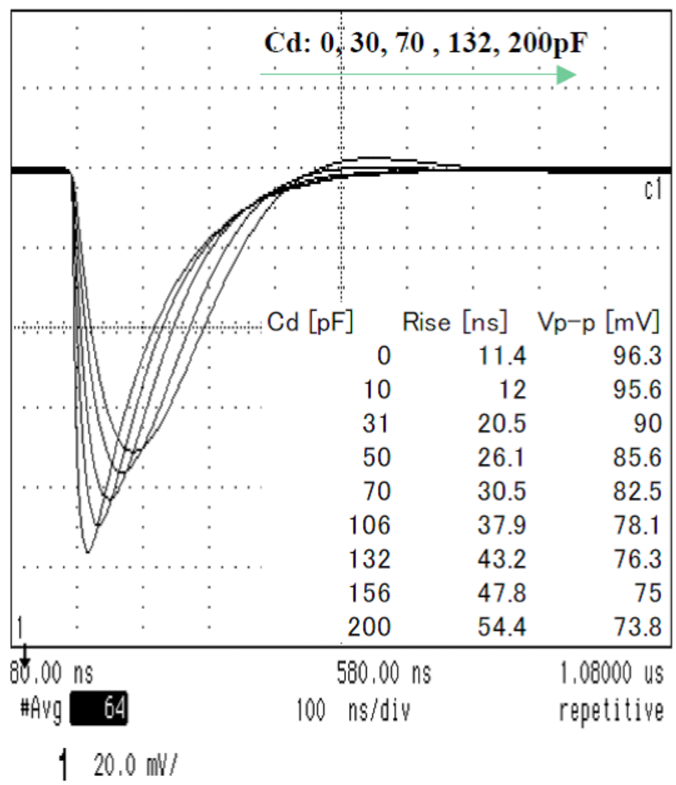

Figure 4.6: The output signals with pseudo detector capacitances of 0, 30, 70, 132, and 200 pF. Test pulse input charge is 0.1pF and its rise time is 5 ns. The horizontal scale is 100 ns/div and the vertical scale is 20 mV/div.

Typical detector capacitance is ∼70 pF. With a pseudo detector capacitance of ∼70 pF and test pulse input charge of 0.1pF whose rise time is 5 ns, we observe the rise time of 31 ns and the output amplitude of 83 mV. The charge gain is calculated to be 0.8 V/pC, which is smaller than the design value, 1 V/pC (the feedback capacitance is 1pF). This is because the open loop gain of the preamplifier is not large enough and the waveform is distorted.

Equivalent Noise Charge

Fig. 4.7 shows the Equivalent Noise Charge (ENC) with various pseudo detector capacitances. Fitting with a theoretical function, ENC is ∼3300 electrons, with the pseudo detector capacitance of 70 pF. This is consistent with the estimated value, 2900 electron, calculated using data sheet parameters of the input transistor.

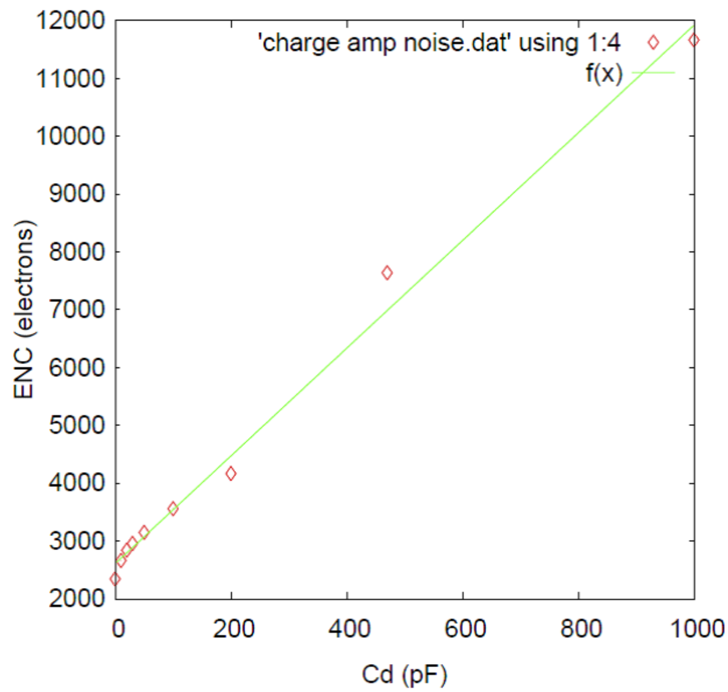

Figure 4.7: The Equivalent Noise Charge (ENC) vs. pseudo detector capacitance.

Slew rate

As the input charge increase, the waveform of the output signal is distorted by the slew rate limit before the saturation of the the output signal amplitude occurs (See Fig. 4.8), with the test pulse rise time of 5 ns and the pseudo detector capacitance of 70 pF. The observed slew rate is ∼50 V/μsec. When the detector capacitance is

70 pF, the width of the detector raw signal is 5 ns, and the rise time of the output signal is 30 ns, the slew rate limit of the preamplifier is given as $(30\,ns/0.8)\times 50\,V/\mu$sec $=1.9$ V[c]. Assuming that the detector gain is 10^5 and all the charge generate by the detector flows into the preamplifier, the slew rate limit in photoelectron (p.e.) is given as follows:

$$\frac{1.9V}{1.6\times 10^{-19}\,C\times 10^{5}\times 0.8\,V/pC} =\sim 150\,p.e. \tag{4.3}$$

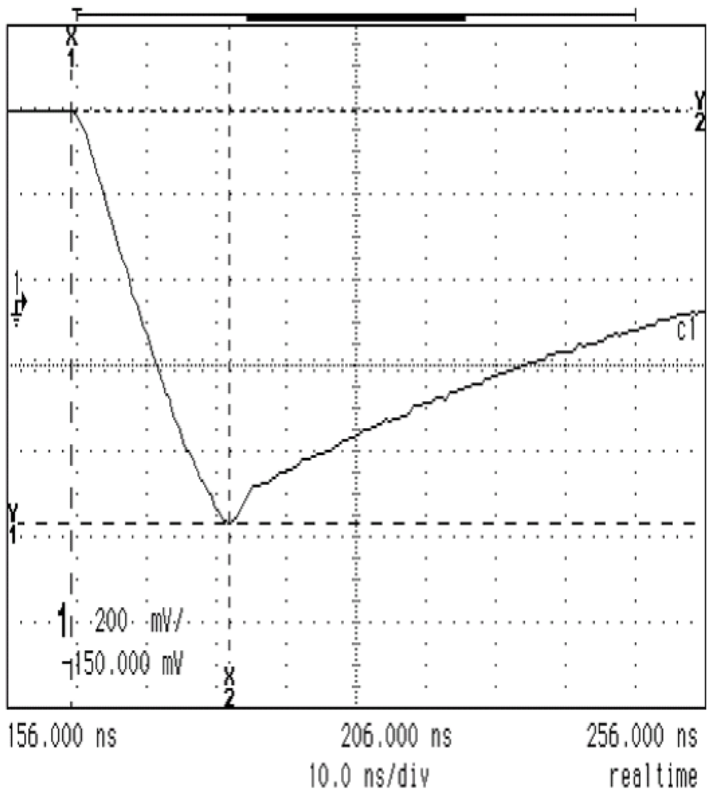

Figure 4.8: The figure shows the output signal of the discrete circuit preamplifier, distorted by the slew rate limit. We observe the slew rate of $\sim$50 V/μsec. The horizontal scale is 10 ns/div and the vertical scale is 200 mV/div.

We suppose the cause of the slew rate limit is the stray capacitance in the circuit(See Fig. 4.9). When v in Fig. 4.9 drops, the stray capacitance must be discharged first. Therefore, the slew rate of the preamplifier is determined by I/C.

[c]The definition of the rise time is 10%-90%.

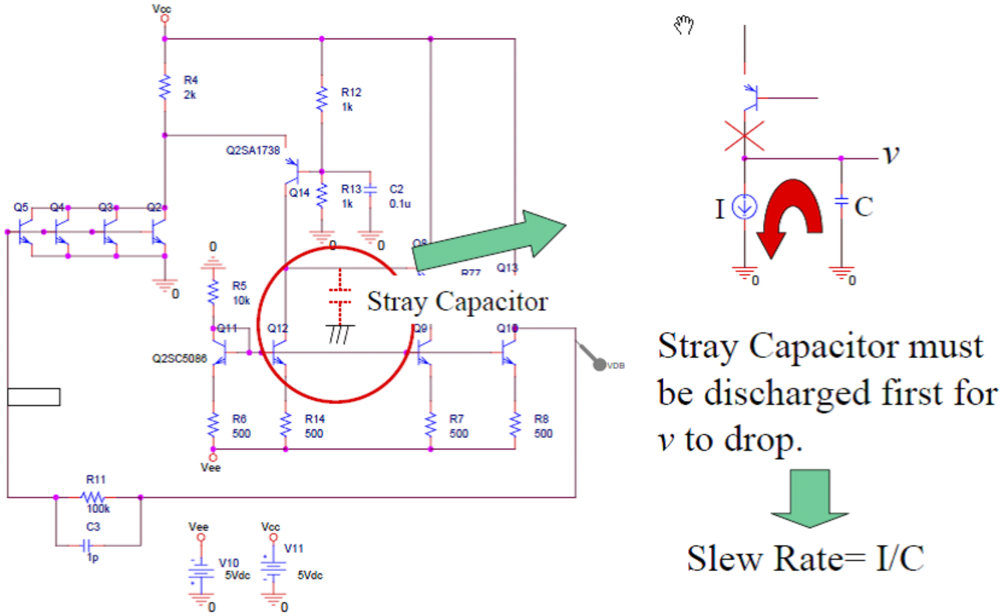

Figure 4.9: The slew rate is limited by the stray capacitance in the circuit.

Linearity

Fig. 4.10 shows the saturation of the output signal and the linearity of the preamplifier. The rise time of the input signal is set to be long so that slew rate does not limit the output signal. The linearity holds up to the output signal amplitude of $\sim$1.4 V with a resolution of $\sim$7 bit. (See Fig. 4.15 for the residuals of the linear fit). The linearity limit is equivalent to $\sim$125 p.e., assuming that the detector gain is 10^5 and all the charge flows into the preamplifier. Since this is smaller than the slew rate limit with the same assumption as above, 150p.e., the linearity limit determines the dynamic range of the preamplifier.

4.2.4 ASIC2004

Fig. 4.11 schematically shows the ASIC preamplifier, version "ASIC2004." This ASIC preamplifiers are fabricated using the bipolar process (NEC, 0.6 μm). We use ten transistors in parallel as the input transistor. The feedback capacitance is 1pF, and the feedback resistance is 100kΩ.

Note that feedback capacitor is not in parallel with the feedback resistor, but one of its terminals is connected to the middle node of the signal path. This method has two merits in stabilizing the circuit. First, the fast feedback capacitor works as the capacitor for "compensation." Since the input side of the feedback capacitor's terminal is almost fixed at a constant voltage, the feedback capacitor reduces the

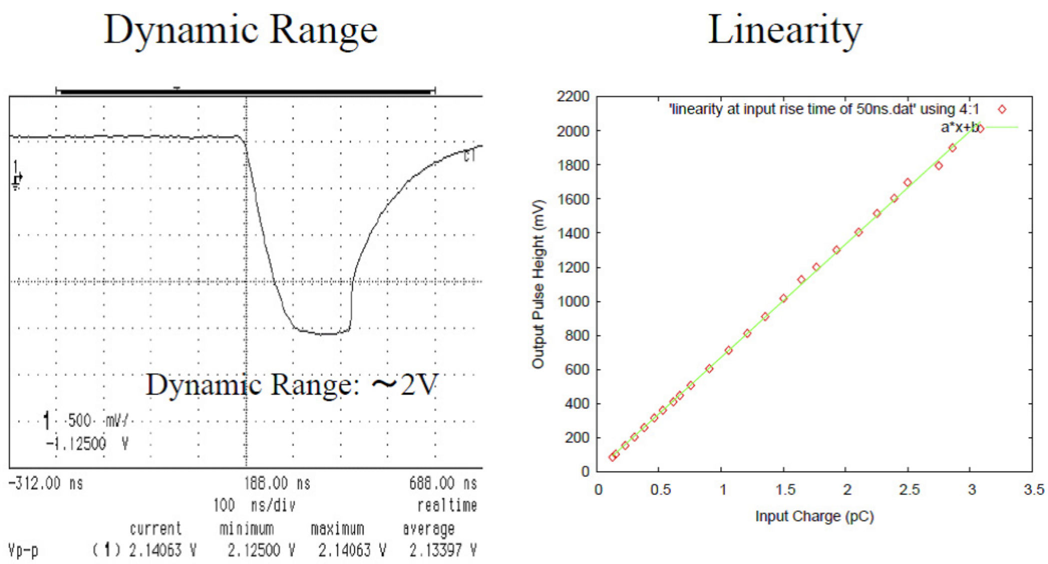

Figure 4.10: The left figure shows the saturation of the preamplifier output. The horizontal scale is 100 ns/div and the vertical scale is 500 mV/div. The right figure shows the linearity of the discrete circuit preamplifier, fitted with a linear function.

bandwidth of the preamplifier, and we can decrease the feedback amplitude in a high frequency region where the stability is not good. This is called "compensation." Second, the feedback current through the feedback capacitor is namely faster than that in the normal feedback configuration. The faster feedback current is, the better the circuit is stabilized.

Detector capacitance dependence of the impulse response

Fig. 4.12 shows the output signals with various pseudo detector capacitances connected in parallel with the preamplifier input. The ASIC preamplifier shows less waveform deterioration than discrete circuit preamplifier, because the open loop gain of the ASIC preamplifier is greatly improved compared to that of the discrete circuit amplifier.

Typical detector capacitance is $\sim$70 pF. With a pseudo detector capacitance of $\sim$70 pF and the test pulse input charge whose rise time is 5 ns, we observe the rise time of 5 ns and the charge gain of 0.6 V/pC, which is smaller than the designed value, 1 V/pC (the feedback capacitor is 1 pF), even though the open loop gain is large enough (no deterioration of the output waveform is observed with C_d=70 pF). We also found that the time constant of its tail is $\sim$200 ns, which is longer than the design value,100 ns (1 pF$\times$100kΩ). Therefore we assume that we have the wrong feedback capacitance of $\sim$2 pF, not the design value of 1 pF, because of the process

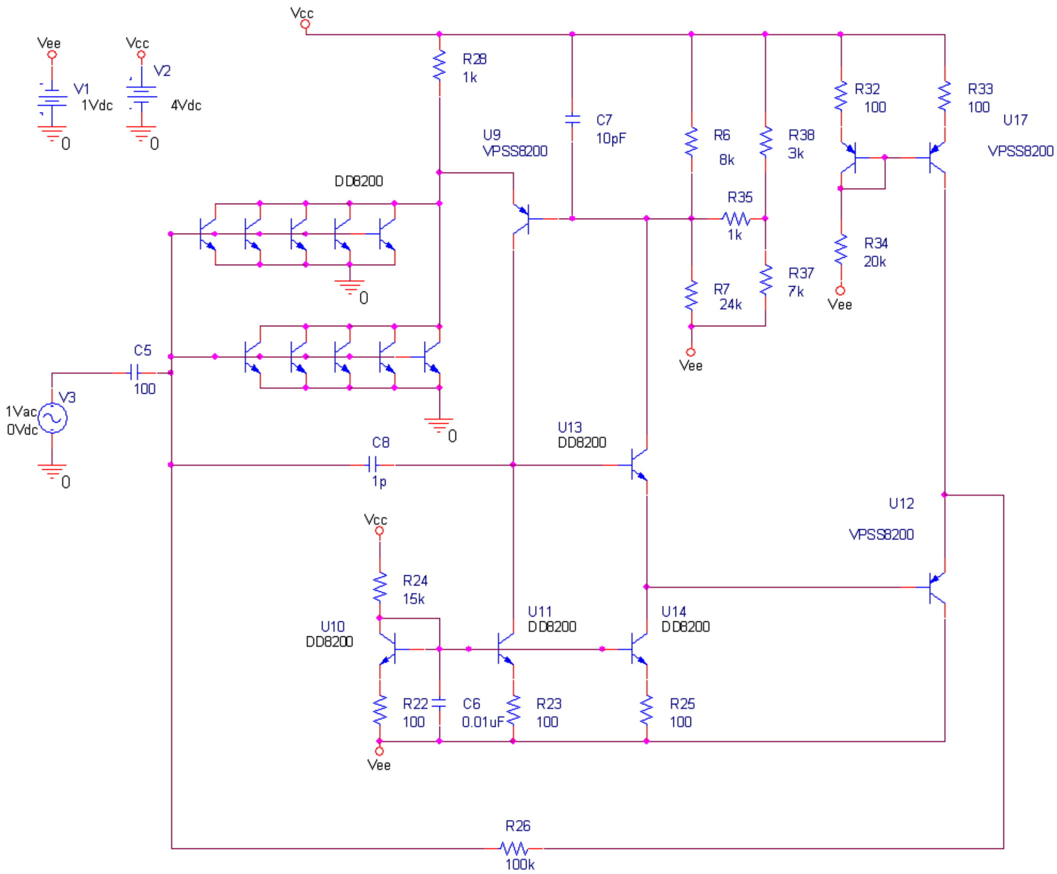

Figure 4.11: The schematic figure of ASIC2004 preamplifier. The feedback capacitor is 1 pF and the feedback resistor is 100kΩ.

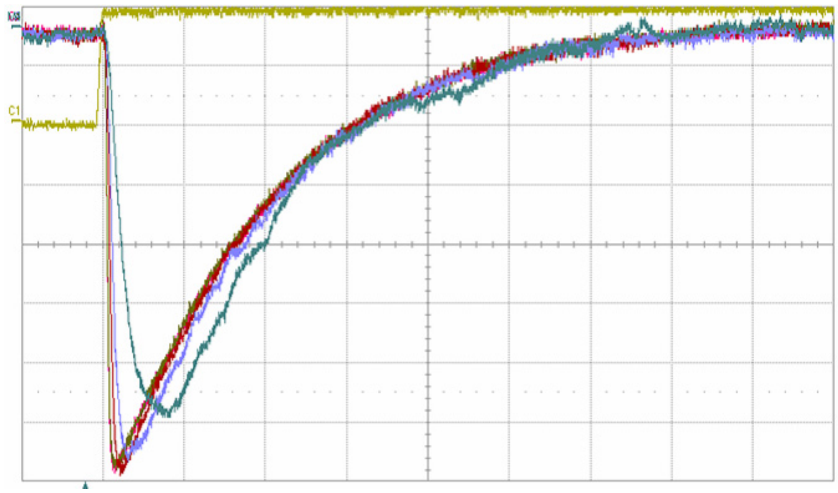

Figure 4.12: The output signals with pseudo detector capacitances of 0(brown), 70(red), 160(blue), and 510 pF(green). The horizontal scale is 100 ns/div and the vertical scale is 20 mV/div.

error and/or the wrong stray capacitance around the feedback capacitor.

Equivalent Noise Charge

Fig. 4.13 shows the Equivalent Noise Charge (ENC) with various pseudo detector capacitances, compared with that of the discrete circuit amplifier. Fitting with theoretical function, ENC of the ASIC2004 preamplifier is ∼3700 electrons with a pseudo detector capacitor of 70 pF. Though it is larger than that of the discrete circuit preamplifier, 2900 electrons, it is still smaller than the requirement value of 10^4 (the typical HAPD gain is 10^5). In addition, since the ASIC preamplifier has wider bandwidth, it is possible that the ASIC preamplifier shows better noise performance than discrete circuit preamplifier, after the application of the digital filter.

Slew rate

As the input charge increase, the waveform of the output signal is distorted by the slew rate limit, before the saturation of the output signal amplitude occurs (See Fig. 4.14), with the test pulse rise time of 5 ns and the pseudo detector capacitance of 70 pF. The observed slew rate is ∼120V/μsec . Assuming that the detector gain is 10^5 and all the charge flows into the preamplifier, the slew rate limit is calculated to be ∼75p.e., using that the charge gain is 0.6 V/pC, detector capacitance is 70 pF, and width of the detector raw signal is 5 ns.

Though the slew rate improves by a factor ∼2 compared to that of the discrete circuit preamplifier, the slew rate limit in photoelectron (p.e.) becomes worse by a

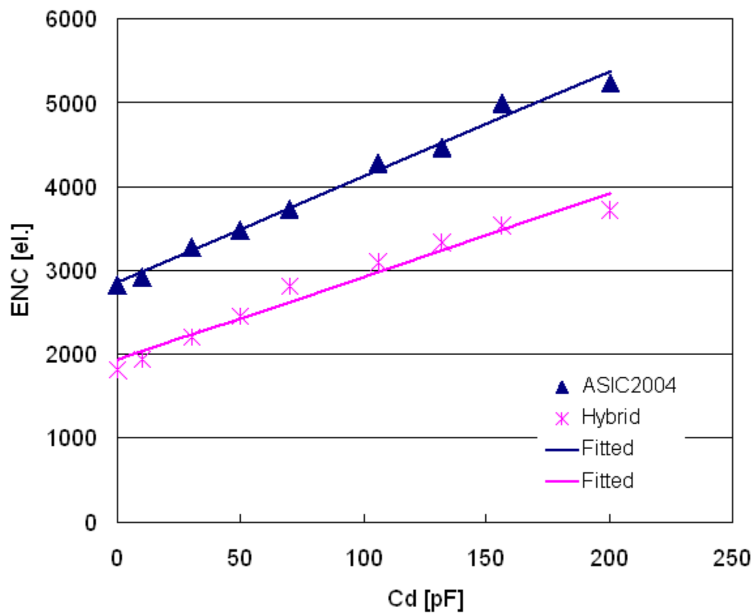

Figure 4.13: The Equivalent Noise Charge (ENC) of ASIC2004 preamplifier, compared with that of the discrete circuit preamplifier.

factor ∼2 because the rise time of the output signal improves and is shorter by a factor of ∼2[d].

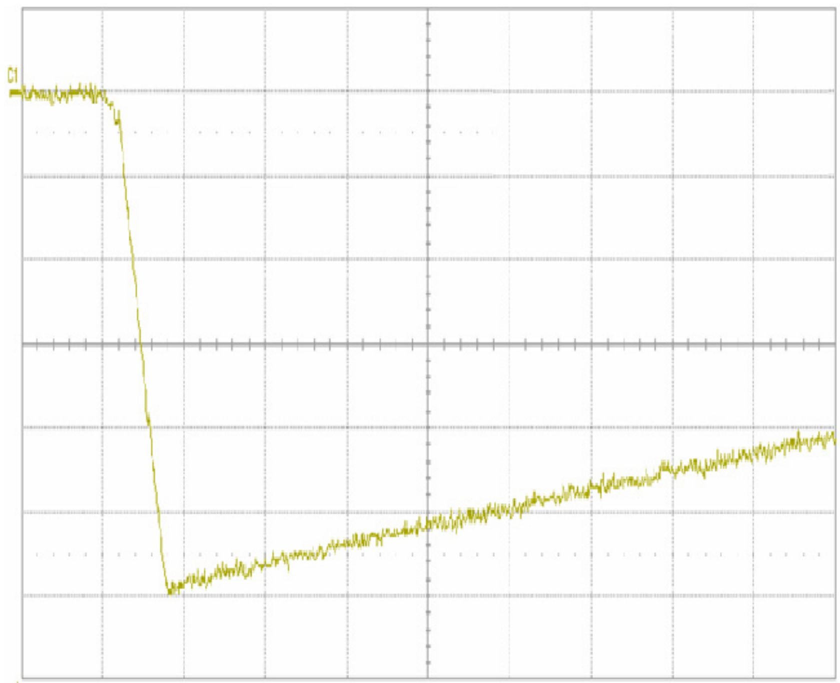

Figure 4.14: The figure shows the output signal of the ASIC preamplifier, distorted by the slew rate limit. The slew rate is ∼120 V/μsec.

Linearity

Fig. 4.15 shows the linearity of the preamplifier. The rise time of the input signal is set to be long so that slew rate does not limit the output signal. The linearity holds up to the output signal amplitude of ∼1.4 V with a resolution of ∼6 bit. The linearity limit is equivalent to ∼100 p.e. This is larger than the slew rate limit, 75p.e., hence in this case the slew rate limit determines the dynamic range of the preamplifier.

4.2.5 Summary and future plans of preamplifiers

Table 4.1 shows the summary of the performance of the preamplifiers. Though ASIC2004 preamplifier meets the requirements of 1. fast rise time (wide bandwidth), 2. no deterioration with pseudo detector capacitance (low input impedance) and 3.

[d] The "slew rate limit in photoelectron (p.e.)" is proportional to the "slew rate " × the "rise time of the output signal ."

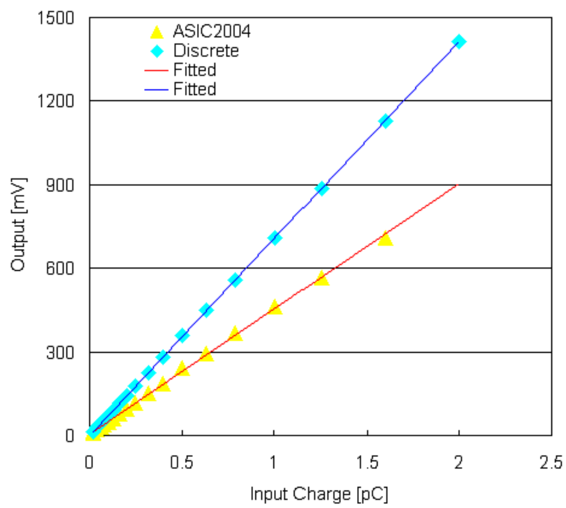

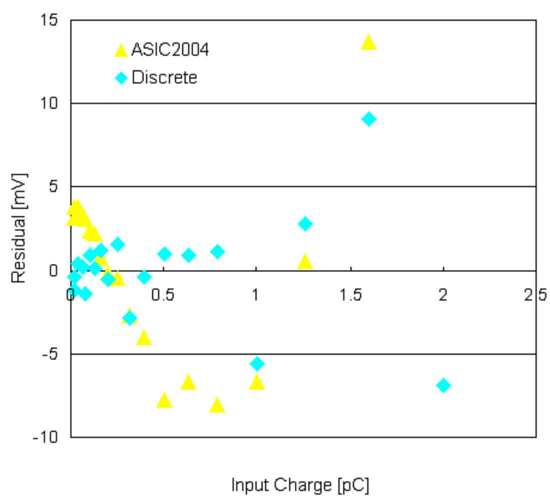

Figure 4.15: The upper figure shows the linearity of the ASIC preamplifier compared with that of the discrete circuit preamplifier, both fitted with a linear function. The lower figure shows the residuals of the fit.

low noise, it doesn't meet the 4th requirement, dynamic range of the preamplifier up to 300p.e.

Our solution to meet the 4th requirement is to use a larger feedback capacitor C_f, which results in smaller charge gain and hence wider dynamic range in photoelectron. As long as $C_{det} \gg C_f$, ENC of the preamplifier is independent of C_f, because ENC is a function of $C_{det} + C_f$.

	Requirements	Discrete circuit	ASIC2004
Wide bandwidth	Rise time $\sim$ 5 ns with C_d=0 pF	$\times$ (8 ns)	$\bigcirc$ (1 ns)
Low input impedance	No deterioration with C_d~70 pF	$\times$	$\bigcirc$
Low noise	ENC $\ll 10^4$	$\bigcirc$ (2900 electron)	$\bigcirc$ (3700 electron)
Linearity and slew rate	Up to ~300p.e.	$\times$ (125p.e., limited by the linearity)	$\times$ (75p.e., limited by the slew rate)

Table 4.1: Summary of the performance of the preamplifiers.

New version of ASIC preamplifier, version "ASIC2005" is under development (it has already submitted). Following issues will be achieved in the new version: 1) modification of the charge gain from 0.6 V/pC to 0.125 V/pC 2) improvement of the slew rate from 120 V/μsec to 2000 V/μsec, and 3) two output ports with/without additional $\times 10$ voltage amplifier for small/large input charge(See Fig. 4.16). The dynamic range of the new preamplifier will not be limited by the slew rate, but by the linearity limit or the saturation of the output signal amplitude. By selecting the appropriate output port depending on whether the input charge is small or large, we will be able to achieve the dynamic range of ~1000p.e.

4.3 AMC as a waveform sampler

Requirements to the waveform sampler are as follows:

1. fast sampling speed

   In order to meet the requirement that the readout system must have time resolution of 1 ns, the sampling speed of the waveform sampler must be as fast as ~1 GHz.

2. high resolution

   In order to meet the requirement that the readout system must have dynamic range of 300p.e., resolution of the waveform sampler must be as high as 9-10 bit, because 1p.e. signal should be equivalent to a few bits.

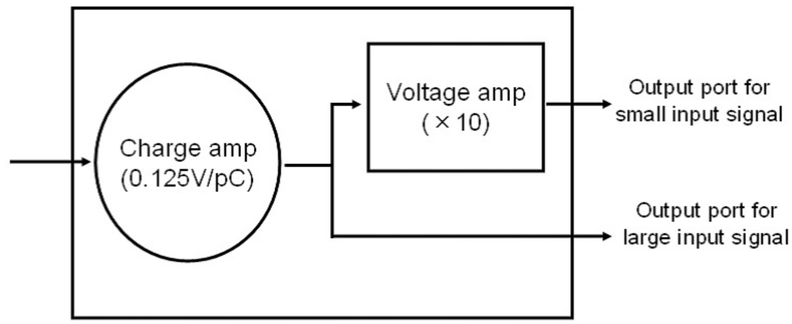

Figure 4.16: The schematic figure of "ASIC2005" preamplifier. Its charge gain is 0.125 V/pC and it has two output ports with/without the additional $\times 10$ voltage amplifier.

As a waveform sampler, there are two possible configurations: fast Flash ADC (FADC), or Analog Memory Cell (AMC) + slow FADC. We develop AMC+slow FADC as a waveform sampler.

First, we describe the principle of AMC. Second, we compare the characteristics of AMC and FADC. Finally, we report the R&D of our AMC, version "AMCM64."

4.3.1 Concept of Analog Memory Cell

The important idea of this device is that fast waveform sampling of $\sim$1 GHz is realized without any fast clock, using cell capacitors as a "pipeline" which store the sampled waveform.

The equivalent circuit of AMC is shown in Fig. 4.17. Each stage consists of an analog switch, a cell capacitor, a delay buffer and an output buffer amplifier. If a trigger signal is injected to the first stage of AMC, the analog switch of the first stage turns off, and after being delayed by the delay buffer, the trigger signal travels to the second stage. In the same way, all analog switches are turned off one by one as the trigger signal go through all stages. When an analog switch of a stage is turned off, voltage of analog input at that timing is "memorized" by the cell capacitor of the stage. As a result, the first cell capacitor memorizes the voltage of analog input at time T_t, the second cell capacitor memorizes the voltage of analog input at time $T_t + t_d$, $\cdots$,and the kth cell capacitor memorizes the voltage of analog input at time $T_t + (k-1)t_d$, where T_t is the triggered time , t_d is the delay time of each delay buffer, $k = 1, 2, \cdots, N$, and N is the number of the stages. N is also called "depth" of AMC. The waveform stored by cell capacitors are read out via an analog multiplexer. Output of multiplexer is AD converted by relatively slow FADC, with sampling speed of few MHz .

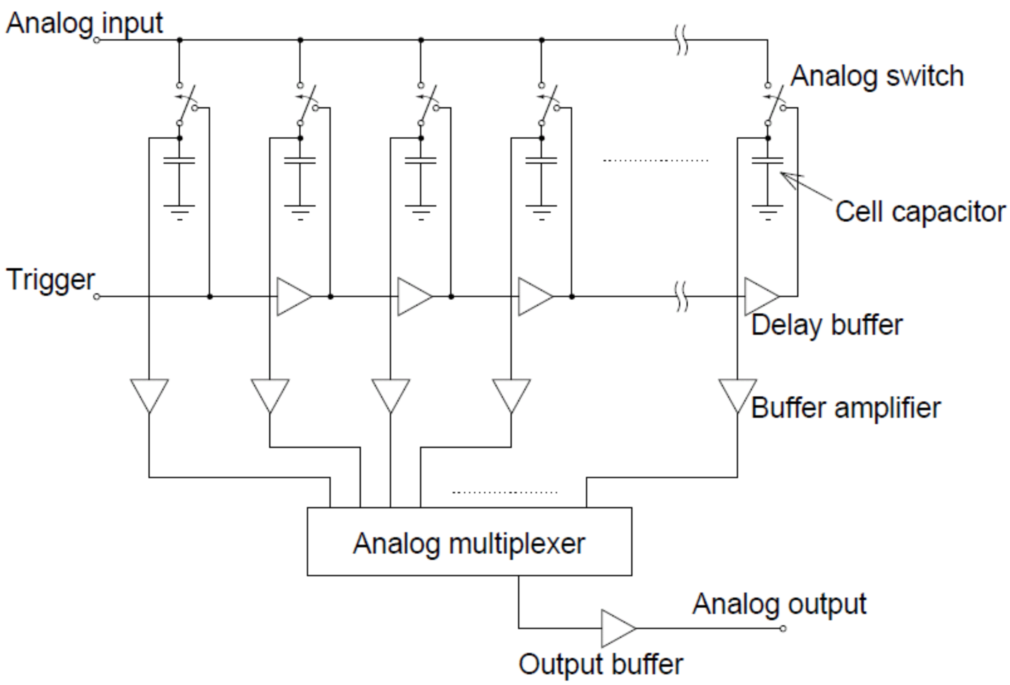

Figure 4.17: The equivalent circuit of Analog Memory Cell (AMC).

4.3.2 Analog Memory Cell and Flash ADC

The characteristics of AMC and FADC are summarized in Table 4.2. The merits of AMC are its low power dissipation and low cost per channel, which are important features in case of large scale experiments. In addition, since AMC is implemented in ASIC, we can put preamplifier and waveform sampler into the same ASIC chip, and we can save space of readout electronics. The demerit is its limited depth, but we can overcome this demerit by connecting multiple AMCs in daisy chain pattern. The primary merit of Flash ADC is that it is already available commercially. The demerit is its large power dissipation and high cost per channel.

As for the resolution, FADCs of ~10 bit resolution are available. However, they are not listed in Table 4.2, since they are too expensive and their power dissipation is too large. Note that cost and power dissipation of FADC are almost proportional to 2^n when it has n bit resolution.

Considering the merits and demerits, we choose AMC as our waveform sampling device.

	AMC	FADC
Sampling speed	1~2 GHz	0.5~1 GHz
Power / channel	≤ 0.5 W	1~2 W
Cost / channel	$\sim 10^4$yen	$(0.5 \sim 1) \times 10^5$yen
Depth	512~1024	$\geq 10^4$
Resolution	≥ 10 bit	~8 bit

Table 4.2: The summary of performance of AMC and FADC.

4.3.3 AMCM64

Fig. 4.18 is the picture of our AMC, version "AMCM64." The number of stages, or its "depth," is 64. It has two blocks and each block contains 32 stages. The sampling speed is designed to be ~1 GHz.

Timing chart

Fig. 4.19 is the timing chart of input/output signal of AMC. At the falling edge of "DIN," AMC starts sampling an input signal. After taking 64 samples, it stops sampling. At the rising edge of "SRDI," stored waveform starts to be read out. At the rising edge of "DIN," all capacitors are discharged. The simplified equivalent circuit (only one stage) is shown in Fig. 4.20.

Linearity

Fig. 4.21 shows the linearity of 1st, 17th, and 32th stage of AMC block 1. We input the constant voltage from the analog input of AMC and measure the output

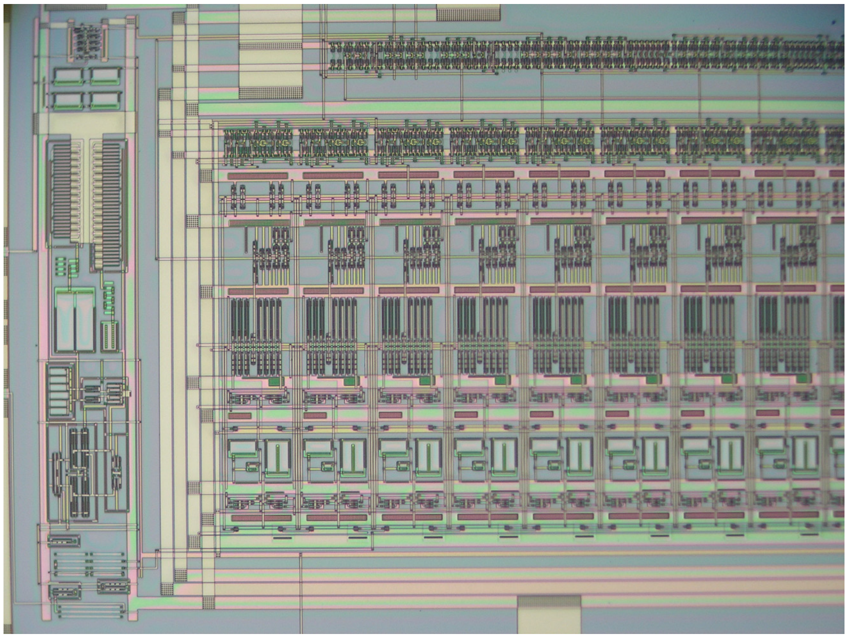

Figure 4.18: The circuit pattern of AMC.

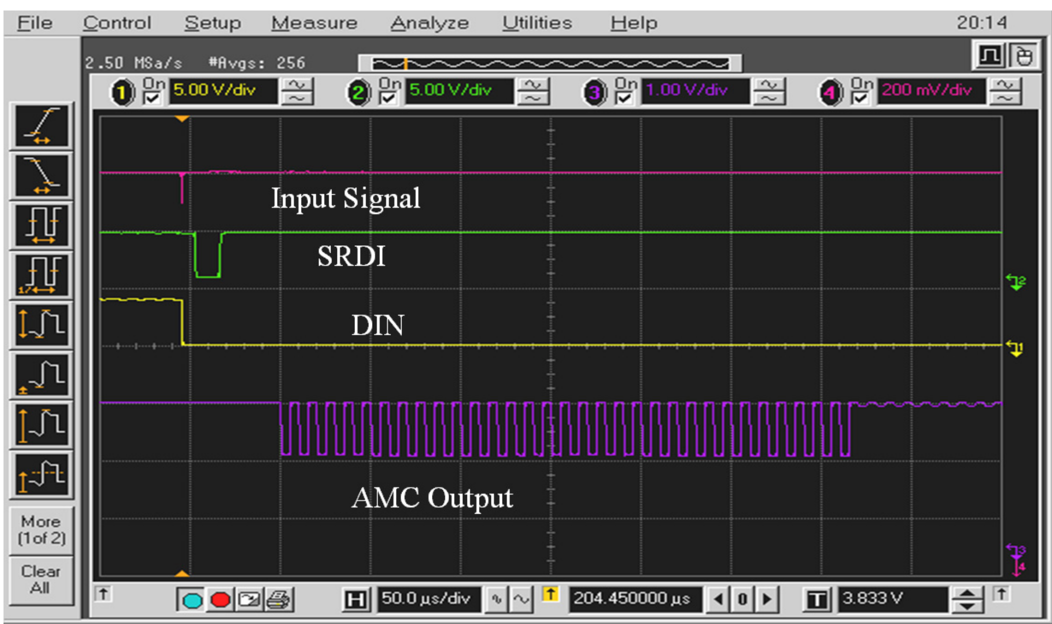

Figure 4.19: The timing chart of AMC. The readout clock is 100kHz.

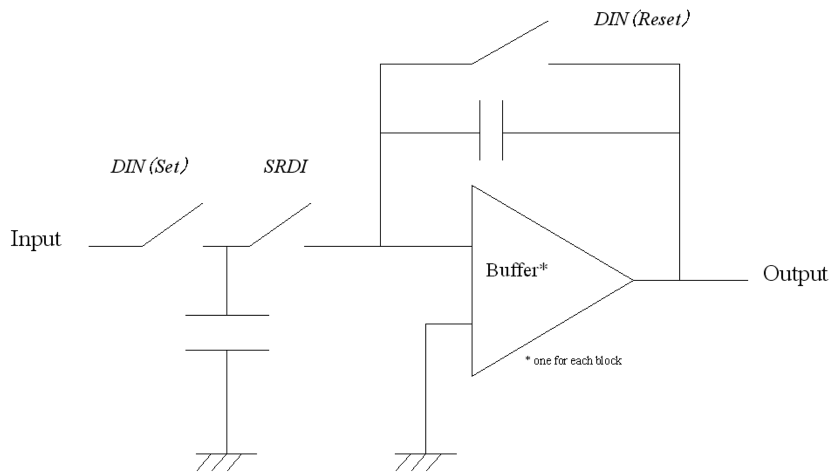

Figure 4.20: The equivalent circuit of one cell of AMC.

level, varying the input voltage. Each stage has the dynamic range of ∼5 V and the linearity holds within the dynamic range, with the resolution of ∼8 bit. This doesn't satisfy the requirement. Note that the resolution of AMC is worse than that of each stage of AMC, due to the effect of stage by stage dispersion shown in the next section.

Stage to stage variation of output amplitude

Fig. 4.22 shows the output signal of AMC block 1 (2), when we input the constant voltage of 1 V (-1 V), respectively. Fig. 4.23 shows the differences of the output amplitudes of AMC block 1, when we input the constant voltage of -2.9 V∼2.1 V. We observed the output amplitude differs ∼40mV.

Propagation delay interval between stages

Fig. 4.24 shows the delay interval of the delay buffers of each stage. We measure the delay interval between mth stage and nth stage, using a method described below. We use a ramping up signal as a input, with a variable delay. First we set the input delay to be T_d and measure the output amplitude of nth stage, $A(n, T_d)$. Then we change the input delay from T_d to $T_d + \Delta T_d$ so that output amplitude of mth stage is equal to be $A(n, T_d)$,

$$A(m, T_d + \Delta T_d) = A(n, T_d). \tag{4.4}$$

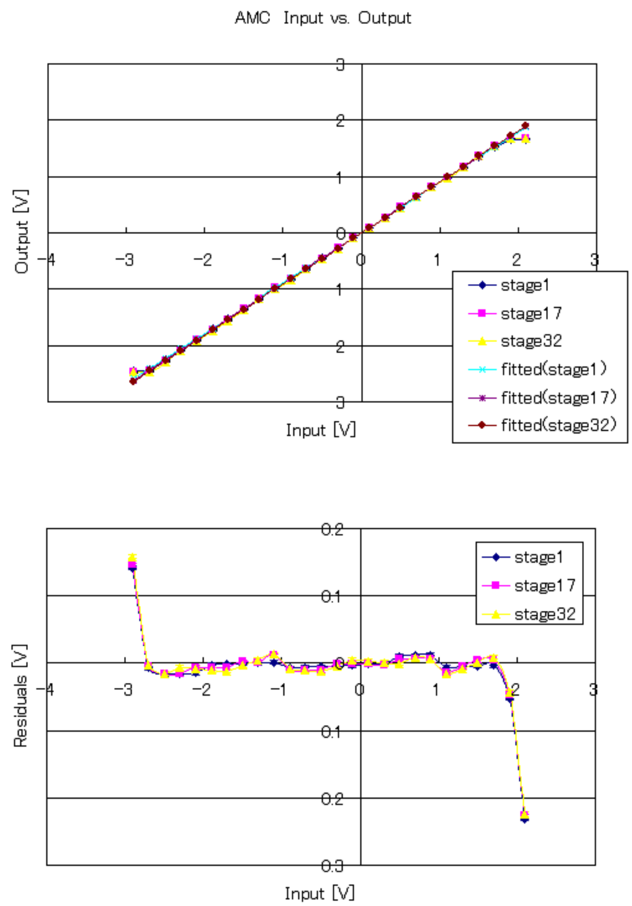

Figure 4.21: The upper figure shows linearity of 1st, 17th, and 32th stage of AMC block 1, fitted with a linear function. We use the data of input voltage = -2.7∼1.9 V for the fit. The lower figure shows the residual of the fit.

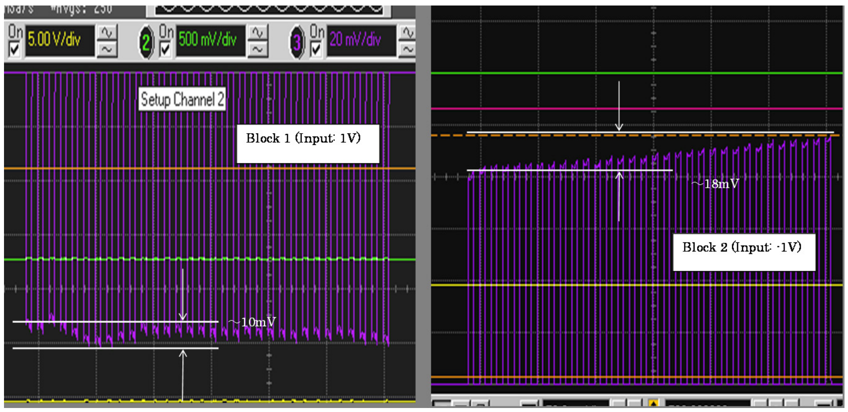

Figure 4.22: The left (right) figure shows the output signal of block 1 (2), with the constant voltage input of -1 V (1 V). The dispersion is ~10 mV (~20 mV), with the constant voltage input of -1 V(1 V).

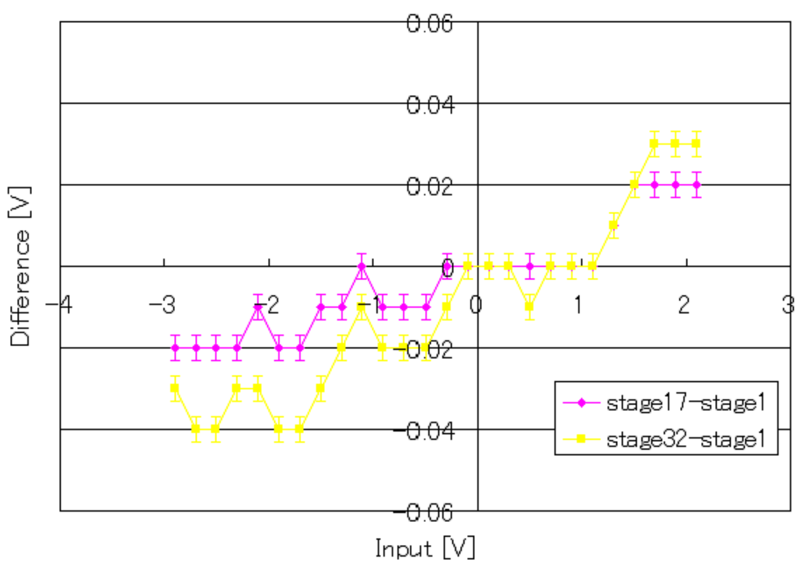

Figure 4.23: The differences of the output amplitudes of AMC block 1. The amplitude differs ~40 mV.

Here, ΔT_d is a delay interval between mth and nth stage (See Fig. 4.25).

The dominant sources of errors in Fig. 4.24 are as follows: 1) The minimum step of the delay is 50ps. This results in the error of $\sigma = 50/\sqrt{12} = 15\,\text{ps}$. 2) We use the input signal with a rise time of 5 ns and amplitude of 2 V. As the output amplitude could vary ∼10 mV, with a input voltage of 1 V, depending on which stage we are measuring (See Section 4.3.3). This results in the error of ∼25 ps.

The tendency is observed that the former stages have smaller delay in both blocks. We suspect this is because the circuit layout of the current AMC is not appropriate and the ground impedance of the stage is not small enough. This problem will be solved in the next version of AMC, by making the ground impedance small enough with careful circuit layout.

Pulse response

Fig. 4.26 shows the AMC response to the fast pulse input, varying the input delay. We observe deterioration of pulse shape[e] , which means the bandwidth of stages is not uniform.

We suspect this is because the circuit layout of the AMC is not appropriate and the ground impedance is not small enough. This problem will be solved in the next version of AMC, by making the ground impedance small enough with careful circuit layout.

4.3.4 Summary and future plans

We have developed an AMC version "AMCM64," which has ∼1 GHz sampling speed and ∼8bit resolution. The stage to stage variation of output amplitude makes the resolution worse.

Though our AMC meets the sampling speed requirement, it fails to meet the requirement of resolution, 9∼10 bit. We also found some problems, stage-to-stage variation of output amplitudes, delay intervals, and bandwidths, due to the inappropriate ground impedance.

For the next versions of AMC, we are planning to 1) modify the circuit layout so that ground impedance is reduced , and 2) improve the resolution to meet the requirement of resolution 9∼10 bit, by improving the linearity. Using AMC in differential mode is also effective for improving the resolution. We also increase the number of stages up to 512∼1024, by implementing many AMCs in series in one chip, in order to achieve a wide time window (0.5∼1 μs) to sample the entire waveform of the preamplifier output signal.

[e] For example, maximum amplitude of the output signal changes, depending on the input delay, or which stage is the maximum.

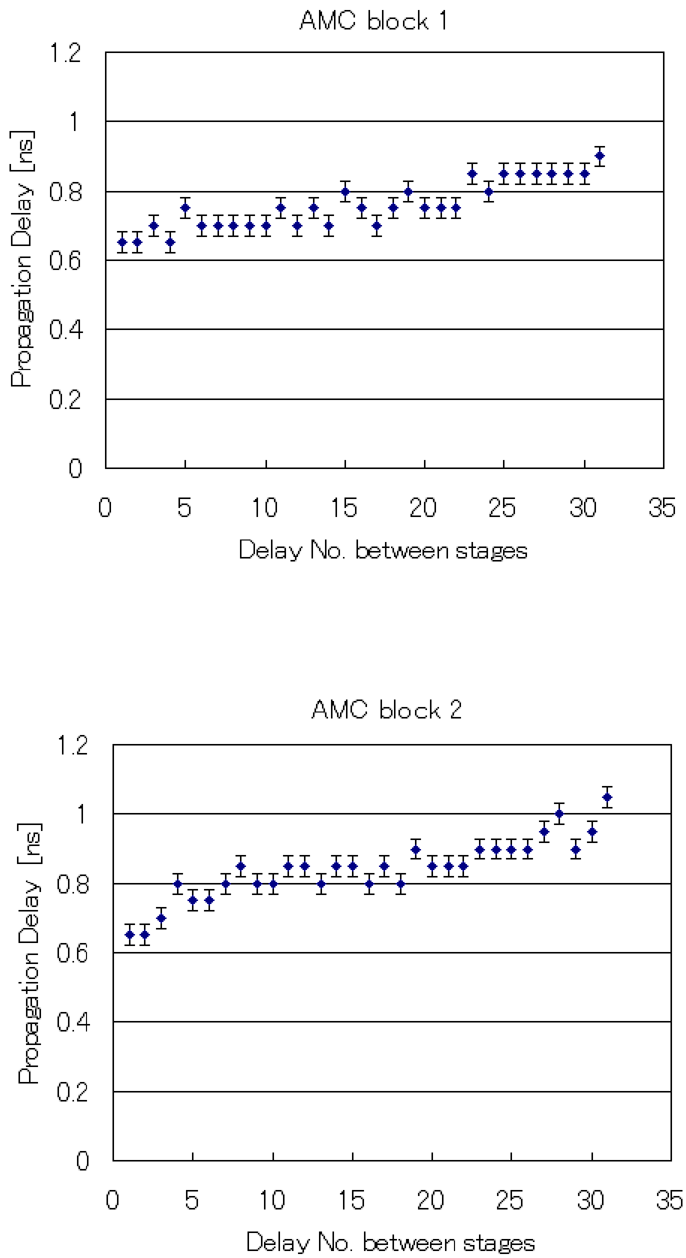

Figure 4.24: The upper (lower) figure shows the delay interval of each stage in AMC block 1 (2).

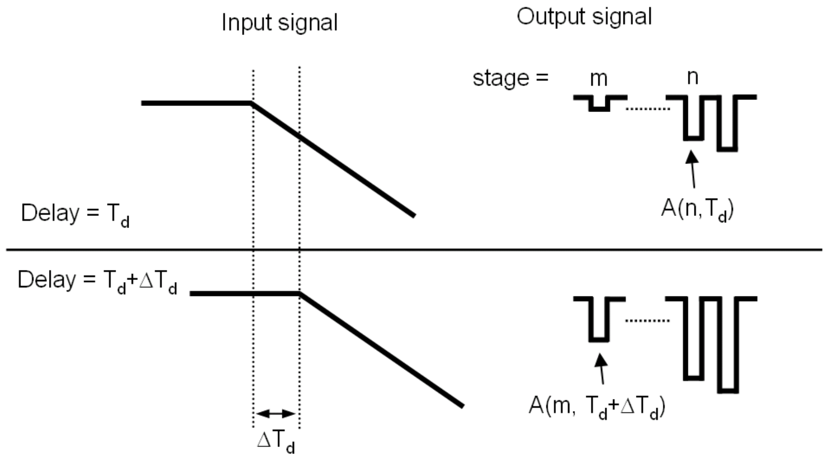

Figure 4.25: How to measure the delay interval of each stage. Delay interval between mth and nth stage is given by ΔT_d when $A(m, T_d + \Delta T_d) = A(n, T_d)$.

4.4 Digital filtering algorithm

We apply digital filter on the sampled and digitized waveform, in order to 1) suppress noise component and enhance signal component , and 2) deduce information of amplitude Q and timing T (see Fig. 4.27).

We adopt Field Programmable Gate Array (FPGA) as a device to implement the digital filtering algorithm. Optimization of the digital filter was done considering not only for performance but also its cost.

First, we describe our digital filter algorithm. Then we describe the R&D of its implementation on FPGA.

4.4.1 Digital filtering algorithm

Digital filters and analog shaping amplifiers

Digital filter is a substitute for a shaping amplifier which is generally used in readout system. A major merit of digital filter is that it is highly customizable and hence gives superior performance. Since HAPDs have relatively small gain, it is important to suppress noise in order to achieve larger S/N ratio for single photon detection and good time resolution. The demerit is the need of a waveform sampler, its cost on implementation, and larger power consumption. However, we can overcome the demerits by using an AMC as a waveform sampler and using FPGA technology for implementation, where the remarkable progress has been made in recent years.

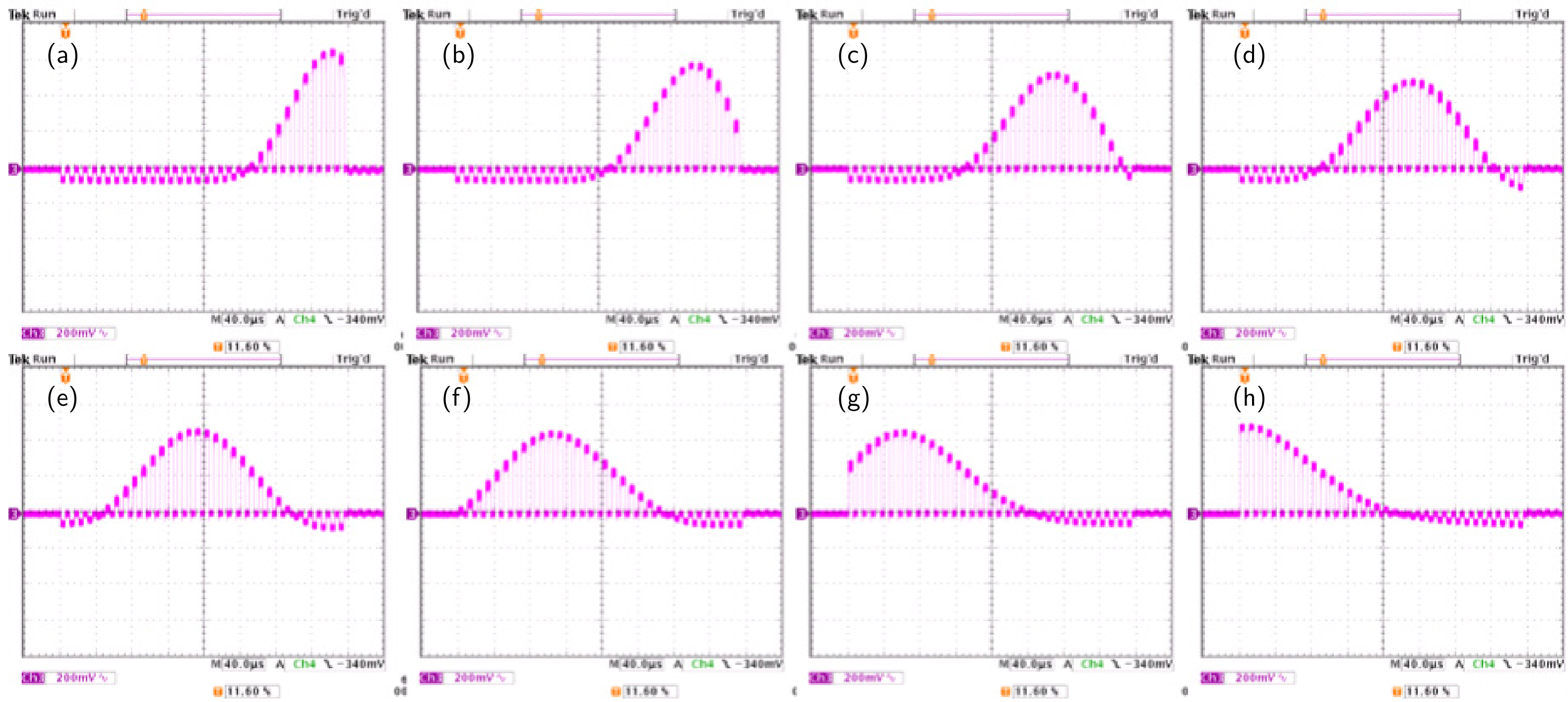

Figure 4.26: The AMC response to the fast pulse input with various input delay. The input delay decreases from (a) to (h).

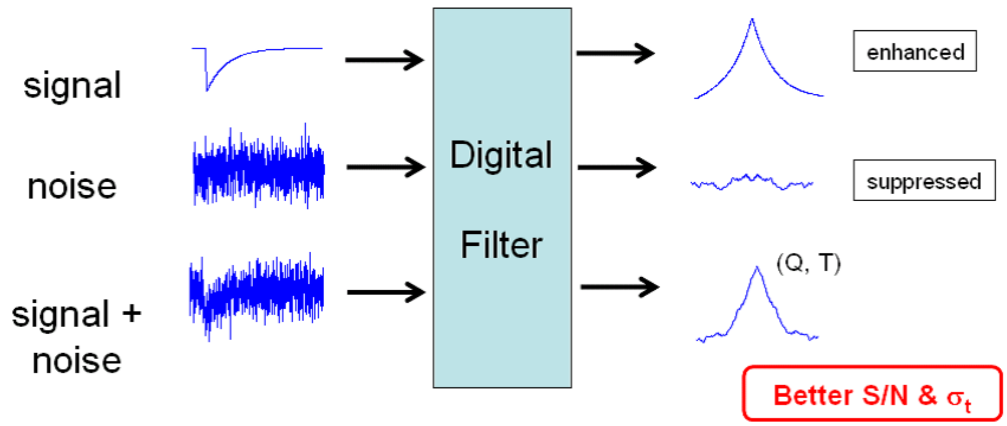

Figure 4.27: The task of the digital filter.

Principle of digital filters

We adopt FIR(Finite Impulse Response) filters. The filter output signal $y[i]$ is calculated from the input signal $x[i](i = 1, \cdots, N; N$ is the length of $x[i])$ as:

$$y[i] = \sum_{j=0}^{L-1} x[i+j] \times h[L-1-j] \tag{4.5}$$

where $h[i](i = 1, \cdots, L)$ is a series that defines the property of the filter and L is the length of $h[i]$. $h[i]$ is called "filter kernel." The equation 4.5 can be written using convolution as:

$$y[i] = (x \otimes h)[i]. \tag{4.6}$$

Using a Discrete Fourier Transformation (DFT), frequency domain expression of $x[i]$, $X[k]$, is given as:

$$X[k] = \sum_{j=0}^{N-1} x[j]e^{-2\pi i \cdot jk/N}. \tag{4.7}$$

Y[k] and H[k] are defined in the same way. Using Convolution Theorem, the equation of the time-domain can be written in the frequency-domain as

$$Y[k] = X[k] \times H[k]. \tag{4.8}$$

Thus, by moving from the time-domain to the frequency-domain, convolution changes into multiplication. Fig. 4.28 shows what happens in the time-domain and the frequency-domain. By changing $H[k]$, we can make any kind of filters such as high pass, low pass, band pass, and so on.

Deduction of amplitude Q and timing T is very simple. We search a peak in $y[i]$. If the peaking time is $i = i_{max}$ and the peak amplitude is $y = y[i_{max}]$, Q, T

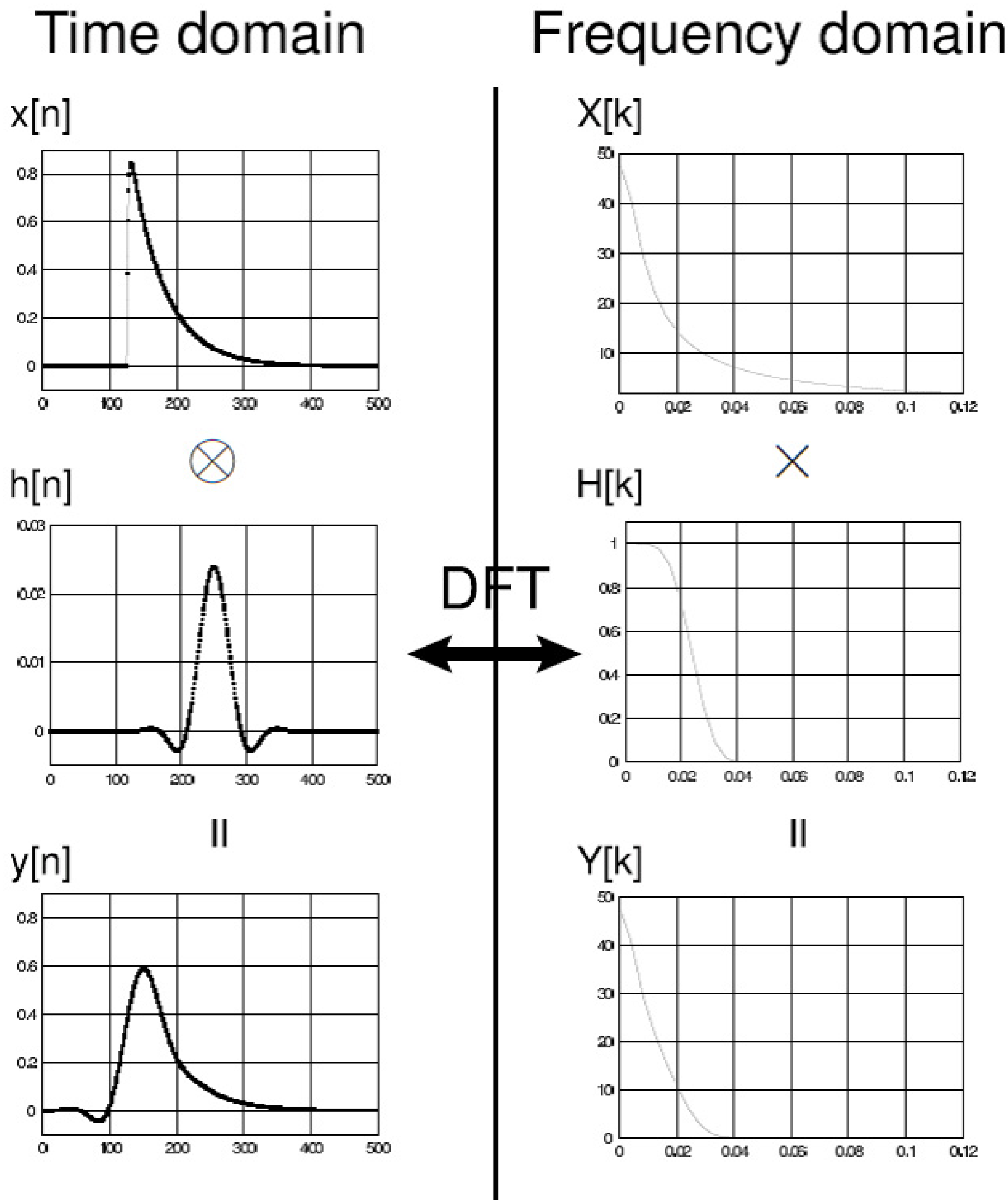

Figure 4.28: An example of the effect of the digital filter in the time-domain and the frequency-domain.

are given as

$$Q \equiv y[i_{max}] \tag{4.9}$$
$$T \equiv i_{max}. \tag{4.10}$$

Q is relative value, and should be calibrated to "number of electrons," using a test pulse input.

For a given set of sampled waveforms and the filter kernel $H[k]$, we can deduce (Q, T) pairs in this way. By making histograms of Q and T, we get the pulse-height spectrum and timing distribution such as Fig. 3.9 and Fig. 3.10, respectively.

Matched Optimal Filter (MOF)

For a given set of $\{x_l[i]\}$ and $\{x_l^{noise}[i]\}$, a digital filter $h(k)$ which gives the best S/N ratio and best time resolution is given by the following equation, where $\{x_l[i]\}$ ($\{x_l^{noise}[i]\}$) ($l = 1, \cdots, N_{event}; i = 1, \cdots, N$) are filter input waveforms with (without) light input, N_{event} is the number of events, and N is the length of waveforms:

$$h(k) = \mathrm{DFT}^{-1}(H(k)),\ H[k] = \frac{S[k]^*}{|N[k]|^2}. \tag{4.11}$$

This filter is called "Matched Optimal Filter (MOF)." $S[k]$ and $N[k]$ are derived from $\{x_l[i]\}$ and $\{x_l^{noise}[i]\}$ [f]. Since the length of $S[k]$ and $N[k]$ is N, the length of MOF is **N**.

In general, signal component distributes mainly in a low frequency region while noise component distributes in almost all frequency region ("noise floor"). In this case, MOF is a kind of low-pass filter. It enhances low frequency region where signal component is dominant and it suppresses high frequency region where noise component is dominant (see Fig. 4.29).

4.4.2 FPGA implementation

We implement the filtering algorithm on Field Programmable Gate Array (FPGA). The important R&D issue is to develop a kernel with shorter length, which is cheaper to implement on FPGA, without losing the performance of MOF.

[f] $x_l[i]$ and $x_l^{noise}[i]$ are expressed as:

$$x_l[i] = s_l[i] + n_l[i], \tag{4.12}$$
$$x_l^{noise}[i] = n_l[i]. \tag{4.13}$$

where $s_l[i](n_l[i])$ are signal(noise) components of the filter input waveform. Assuming that there is no timing correlation between signal and noise, average of $\{n_l[i]\}$ over l is $\sim$0, and DFT of the average of $\{x_l[i]\}$ over l gives the signal frequency distribution $S[k]$, while average over l of magnitude of the DFT of $\{x_l^{noise}[i]\}$ gives the noise frequency distribution $N[k]$.

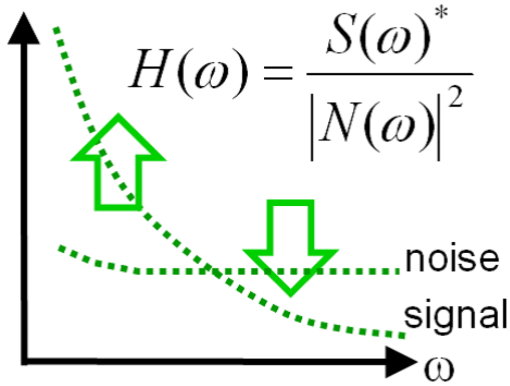

Figure 4.29: How MOF works in the frequency-domain. MOF picks up the low frequency region and suppresses the high frequency region.

Resource consumption on FPGA vs. filter kernel length

To estimate the needed size of FPGA as a function of filter kernel length, we use software tools called "ISE Foundation" and "Xilinx LogiCORE" developed by Xilinx, Inc[g]. ISE Foundation is the integrated softwares to synthesize a bitstream from VHDL files, find an adequate mapping and implement the bitstream onto the device. Xilinx LogiCORE is a set of IP cores, which is highly parameterizable, area efficient and high-performance algorithms to realize a small space consumption and good timing characteristics when implemented onto FPGA. As a FIR filter, we use a IP core called "Distributed Arithmetic FIR."[46] We use the input signal of 10bit, filter coefficients of 10bit and "×11 over sampling" option.

Fig. 4.30 shows the number of needed gates and the price of the corresponding size of FPGA, as a function of the filter kernel length. The number of gates is almost proportional to the filter kernel length. The cost of the FPGA is almost proportional to the filter kernel length. We have two versions of FPGA, "Vertex-II" series and its low-cost version, "Spartan-3" series.

Filter performance vs. filter kernel length

Simulation setup To evaluate the filter performance as a function of filter kernel length, we use a simulation setup described as follows (see Fig. 4.32).

Generate HAPD raw signals whose width is ∼ 5ns. Typical preamplifier response waveform has rise time of <1ns and a tail of time constant of 150 ns. Convoluting raw signals and the preamplifier response, we get signal components of the filter input waveforms, $s_l[i]$, where $l = 1, 2, \cdots N_{event}$ (N_{event} is number of generated waveforms) and $i = 1, 2, \cdots N$ (N is number of sampled points in each waveform).

[g] http://www.xilinx.com/

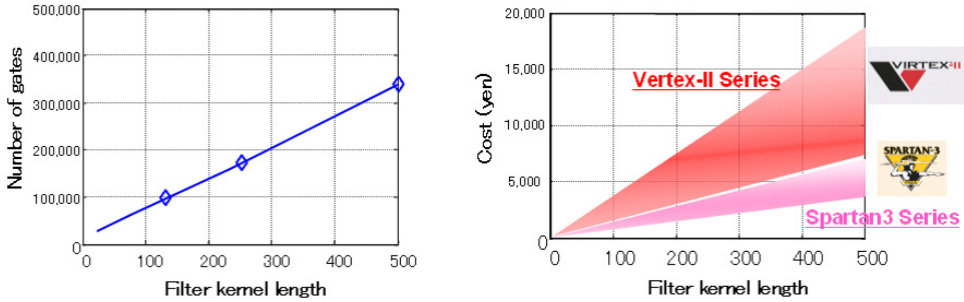

Figure 4.30: The number of gates vs. filter kernel length (left) and cost vs. filter kernel length (right).

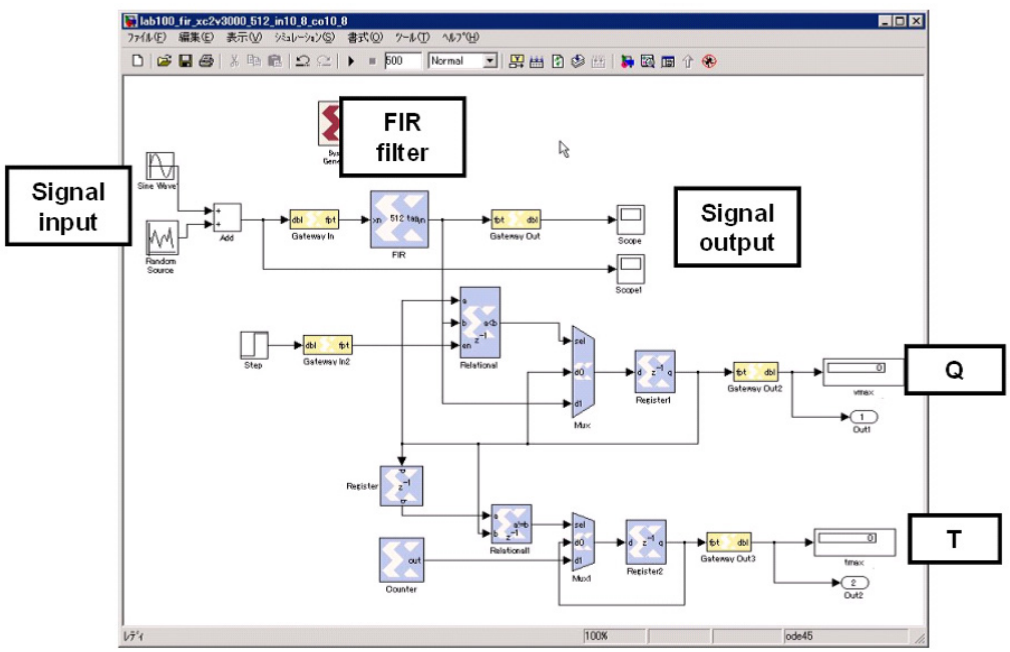

Figure 4.31: The Simulink model of our digital filter.

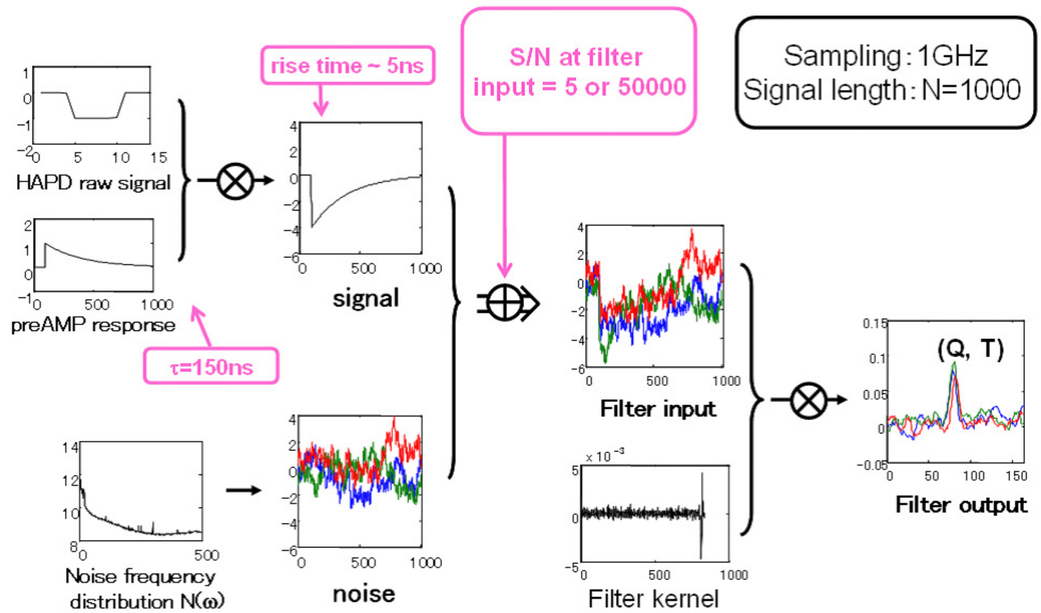

Figure 4.32: The simulation setup.

Generate noise components of the filter input waveforms, $n_l[i]$ from the frequency distribution of the discrete circuit preamplifier noise, $N[k]$. The filter input waveform, $x_l[i]$, is given by adding $s_l[i]$ and $n_l[i]$. When we add $x_l[i]$ and $n_l[i]$, we scale them so that S/N ratio at a filter input is 5 [h] or 50,000.

Assuming that there is no timing correlation between signal and noise, the average of $n_l[i]$s over l is ~ 0, and DFT of the average $x_l[i]$ over l gives the signal frequency distribution $S[k]$. Thus, from $x_l[i]$s and $n_l[i]$s, which correspond to the filter input waveforms with and without the light input, we can derive $S[k]$ and $N[k]$. From $S[k]$ and $N[k]$, we can calculate filter kernel H[k] of MOF by equation 4.11. As a result, kernel length of MOF is N, the length of the sampled waveform.

Shorten the filter kernel Instead of using MOF, we use the filter kernel that has similar performance and shorter kernel length $N'(N' < N)$, given by either of the following methods:

1. "Cutoff" Cut off the both ends of the MOF kernel and make the new kernel whose length is N'(See Fig. 4.33). Note that MOF kernel is almost flat at the both ends of the filter, so we don't lose the performance so much even though we make it shorter in this way.

[h]This is equivalent to the S/N ratio of $\sim$10(See section 3.3.3).

2. “Resampling” Apply DFT on the MOF kernel and resampling it in the frequency domain so that it consists of N' sample points. [i] Then apply inverse DFT and we get the new kernel whose length is N'(See Fig. 4.34).

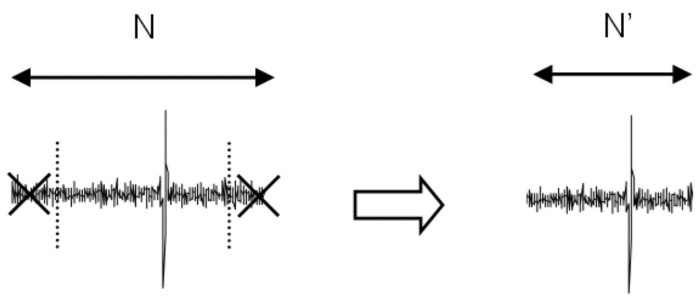

Figure 4.33: “Cutoff” method to shorten the filter kernel length.

The filter length of MOF is ∼1000. Fig. 4.35 and 4.36 show S/N ratio and time resolution after the application of shortened filter kernels, when S/N ratio at filter input are 5 and 50,000, respectively. In the former case, we observe the S/N ratio of ∼10 after the application of MOF. We observe that we can realize almost same performance with MOF, using a filter whose length is 200∼400. This corresponds to the FPGA cost of 2000∼5,000 yen per channel. In the latter case, the time resolution is ∼0.3,ns and equivalent to $1\,\mathrm{ns}/\sqrt{12}$. This shows that the time resolution is limited by the sampling speed.

4.4.3 MATLAB(Simulink)+SignalMaster simulation

Using a software package called MATLAB(Simulink) developed by Mathworks Inc.[j], and the test board called SignalMaster Quad, developed by Lyrtech Inc.[k], we per-

[i] Resample a signal (length p) to make a new signal (length q) is performed as follows. For the given signal $x(i)(i = 1, \cdots, p)$, we apply DFT and obtain $X(j)(j = 1, \cdots, p)$. We define $X'(k)(k = 1, \cdots, pq)$ as

$$\begin{cases} X'(k) \equiv X(k) & \text{if } k = 1, \cdots, p \\ X'(k) \equiv 0 & \text{if } k = p+1, \cdots, pq \end{cases}$$

Then apply inverse DFT and get $x'(k)(k = 1, \cdots, pq)$. The resampled signal $y(j)(j = 1, \cdots, q)$ is given as

$$y(j) \equiv x'(pj)(j = 1, \cdots, q).$$

To avoid aliasing, a low pass filter might be applied to $x(i)$ before the application of resampling.

[j] http://www.mathworks.com/

[k] http://www.lyrtech.com/

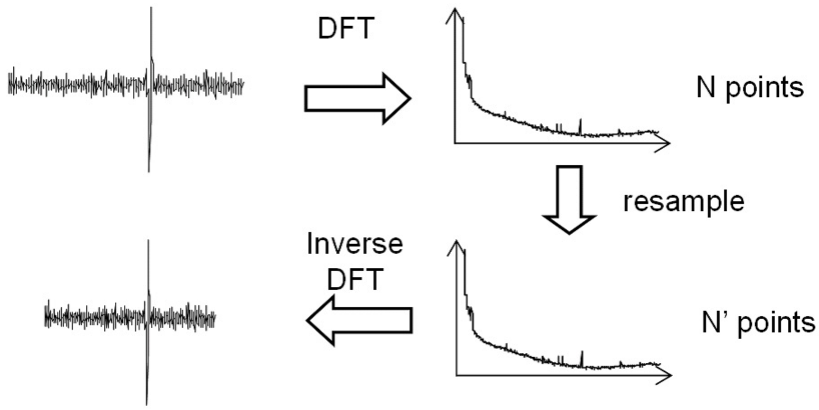

Figure 4.34: “Resampling” method to shorten the filter kernel length.

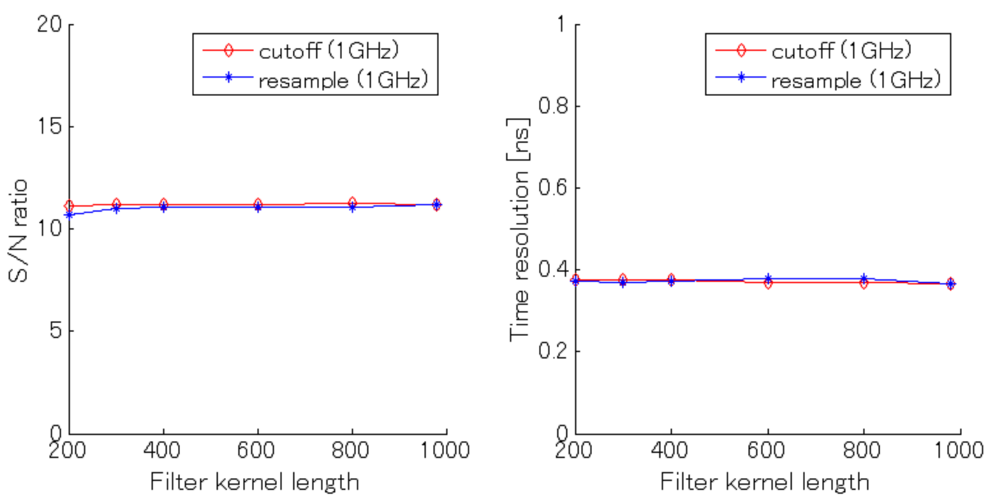

Figure 4.35: The S/N ratio and the time resolution using shortened filter kernel. S/N at filter input is 5.

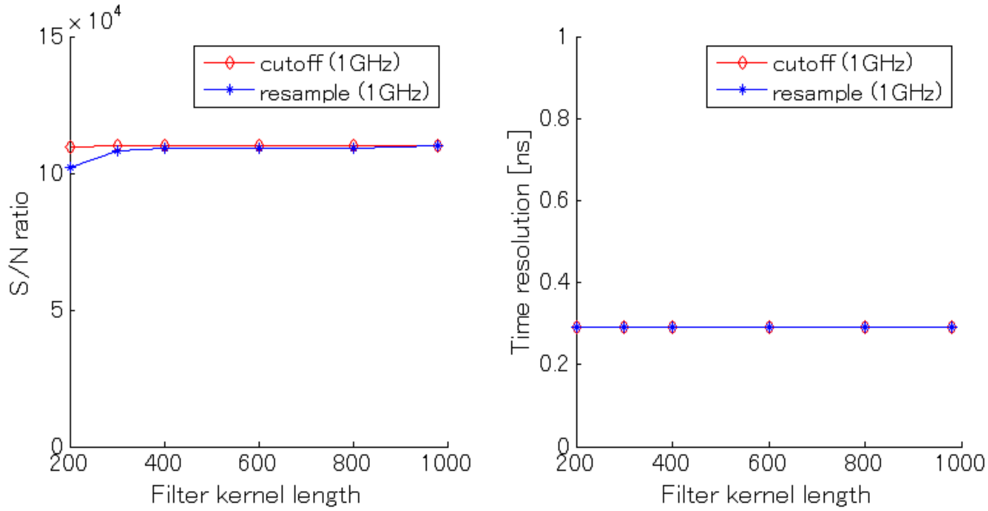

Figure 4.36: The S/N ratio and the time resolution using shortened filter kernel. S/N at filter input is 50,000.

formed the FPGA simulation (See Fig. 4.37). We can perform two types of simulation, host-simulation and co-simulation. In the host-simulation, the structure of the FPGA is perfectly simulated in the Simulink and we can perform the simulation on the host computer. In the co-simulation, the host computer and the FPGA communicate each other. The input signal is generated by Simulink, and passed to the FPGA. The output signal is observed by Simulink. We confirm that our algorithm works properly, in both simulations.

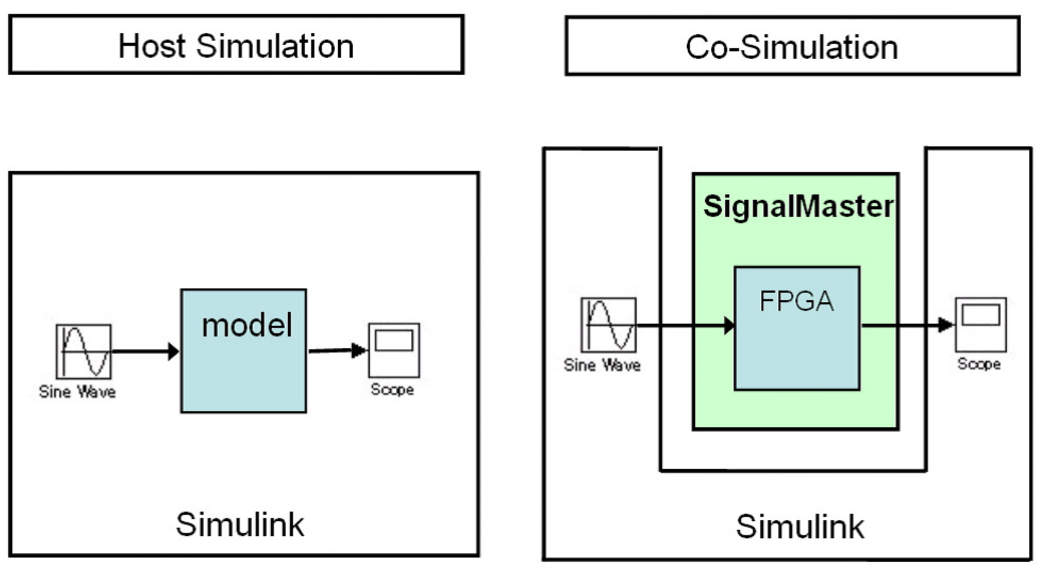

Figure 4.37: Host simulation and co-simulation by MATLAB(Simulink) and SignalMaster.

Chapter 5

Summary and future prospects

5.1 Summary

We have developed a 13-inch prototype HAPD and its readout system. The performance of the HAPD is satisfactory, with a signal speed of $\sim$5 ns, a bombardment gain of $\sim$2,400 and an avalanche gain of $\sim$20. The problem in the HV insulation remains, though. The readout system consists of a preamplifier, a waveform sampler, and a digital filter. The preamplifier is implemented on ASIC. It has wide bandwidth (rise time of $\sim$1 ns) and good noise performance (ENC $\sim$ 3700 for 70 pF detector capacitance). The dynamic range is not satisfactory in the current version of the prototype. As for the waveform sampler, we developed AMC with sampling speed of $\sim$1 GHz and 64 stages. We confirmed the basic behavior of the AMC, but we also found some problems due to inappropriate circuit layout. The digital filtering algorithm has been studied and implemented on FPGA. We estimate the cost of the FPGA is $\leq 0.5 \times 10^4$ yen per channel.

We have evaluated the performance of the HAPD connected with the readout system. The gain is $\sim$24,000, S/N ratio is $\sim$10 and the time resolution is σ=0.7 ns for 1 p.e. equivalent signal. The performance well matched to the requirement for Hyper-Kamiokande.

5.2 Future prospects

The remaining R&D issue for a 13-inch HAPD are wider effective area, better resistance to the water pressure, larger HV decoupling capacitances, and backside illumination ADs.

The next version of the ASIC preamplifier has already been submitted and its dynamic range is expected to satisfy the requirement. The next version of the AMC with careful circuit layout has also been submitted. We are also planning to increase the number of the stage of the AMC up to 512$\sim$1024. We then plan to make a test board on which we can mount ASIC preamplifier, AMC, and FPGA altogether. We plan to confirm that the detector and the readout system works well as a whole system.

Appendix A

Dark count rate

The dominant source of the dark count of HAPD with a large photocathode is electrons emitted from the photocathode. The theories of thermionic and field emission of electrons from metals are very well understood. Following is the discussion taken from [1].

A general expression for the emitted current is given as a function of field, temperature and work function. An approximation of the function for low fields and high temperatures leads to an extension of the Richardson-Schottky formula for thermionic emission. The values of field and temperature for which it applies are established by considering the validity of the approximation. An analogous treatment of the approximation for high fields and low temperatures gives an extension of the Fowler-Nordheim formula for field emission, and establish the region of field and temperature for which it applies.

We assume the potential energy of the electron as follows:

$$V(x) = \left\{ \begin{array}{cl} -e^2(4x)^{-1} - eFx, & \text{when } x > 0, \\ -W_a, & \text{when } x < 0, \end{array} \right. \tag{A.1}$$

where $-e$ is the charge of the electron, $-e^2(4x)^{-1}$ is the contribution from the image force, $-eFx$ is the contribution from the externally applied field F, and $-W_a$ is the effective constant potential energy inside the metal. It is assumed that $V(x)$ is regular and smoothly connected in the region near $x = 0$.

The electric current per unit area is given by

$$\begin{aligned} j(F,T,\phi) = \frac{4\pi mkTe}{h^3}\int_{-W_a}^{W_l} \frac{\ln\{1+\exp[-(W+\phi)/kT]\}\,dW}{1+\exp[(4/3)\sqrt{2}(F\hbar^4/m^2e^5)^{-\frac{1}{4}}y^{-\frac{3}{2}}v(y)]} \\ +\frac{4\pi mkTe}{h^3}\int_{W_l}^{\infty} \ln\{1+\exp[-(W+\phi)/kT]\}\,dW, \end{aligned} \tag{A.2}$$

where

$$W_l = -\frac{\sqrt{2}}{2}(e^3F)^{\frac{1}{2}}, \tag{A.3}$$

$$
\begin{aligned}
y &= (e^3F)^{\frac{1}{2}}/|W|, && \text{(A.4)} \\
v(y) &= -\frac{3i}{4\sqrt{2}}\int_{1-(1-y^2)^{\frac{1}{2}}}^{1+(1-y^2)^{\frac{1}{2}}} [\rho - 2 + y^2\rho^{-1}]^{\frac{1}{2}} d\rho, && \text{(A.5)}
\end{aligned}
$$

m is the electron mass, k is Boltzmann's constant, T is the absolute temperature, h is Planck's constant, and $\phi(> 0)$ is the work function.

In the following discussion, Hartree units are used. That is, j is redefined to mean the current per unit area divided by $m^3e^9\hbar^{-7} = 2.37 \times 10^{14}\,\mathrm{A/cm^2}$; F to mean the electric field strength divided by $m^2e^5\hbar^{-4} = 5.15 \times 10^9\,\mathrm{V/cm}$; and ϕ, kT, W, W_a and W_l to mean the corresponding energies divided by $me^4\hbar^{-2} = 27.2\,\mathrm{eV}$. In these terms,

$$
\begin{aligned}
j(F,T,\phi) = \frac{kT}{2\pi^2}&\int_{-W_a}^{W_l} \frac{\ln\{1+\exp[-(W+\phi)/kT]\}\,dW}{1+\exp[(4/3)\sqrt{2}F^{-\frac{1}{4}}y^{-\frac{3}{2}}v(y)]} \\
&+\frac{kT}{2\pi^2}\int_{W_l}^{\infty} \ln\{1+\exp[-(W+\phi)/kT]\}\,dW. \qquad \text{(A.6)}
\end{aligned}
$$

For low fields and high temperatures, an approximation of Eq. (A.6) leads to

$$
\begin{aligned}
j(F,T,\phi) &= \frac{(kT)^2}{2\pi^2}\left(\exp\frac{F^{\frac{1}{2}}-\phi}{kT}\right) d\int_0^{\infty}\frac{\mu^{d-1}d\mu}{1+\mu} && \text{(A.7)} \\
&= \frac{(kT)^2}{2\pi^2}\left(\frac{\pi d}{\sin(\pi d)}\right)\exp[-(\phi - F^{\frac{1}{2}})/kT], && \text{(A.8)}
\end{aligned}
$$

where $d = F^{\frac{3}{4}}/\pi kT$. The conditions for the applicability of Eq. (A.8) are

$$
\begin{aligned}
\ln[(1-d)/d] - d^{-1}(1-d)^{-1} &> -\pi F^{-\frac{3}{4}}(\phi - F^{\frac{1}{2}}), && \text{(A.9)} \\
\ln[(1-d)/d] - (1-d)^{-1} &> -\pi F^{-\frac{1}{8}}. && \text{(A.10)}
\end{aligned}
$$

Note that when d is so small that $\pi d/\sin(\pi d)$ can be replaced by one, Eq. (A.8) for the current becomes the Richardson-Schottky formula.

In case of our HAPD, $T \sim 300\,\mathrm{K}$, $F < 10^2\,\mathrm{V/cm}$, and $\phi \sim$ few eV. These values satisfy the conditions Eq. (A.9), (A.10) (See Fig. A.1) and the approximation is valid. The conditions are satisfied even if $T = 200\,\mathrm{K}$, $F = 10^3\,\mathrm{V/cm}$, and $\phi = 0.1\,\mathrm{eV}$.

If the effective area of the photocathode is $450\,\mathrm{cm^2}$, $T = 288\,\mathrm{K}$, $F = 70\,\mathrm{V/cm}$, and ϕ=1.5 eV (2.5 eV), the electron emission rate is $1.8 \times 10^2\,\mathrm{Hz}(5.7 \times 10^{-16}\,\mathrm{Hz})$. The dark count rate is the product of the electron emission rate and the collection efficiency.

Dependencies of the emission rate on F, ϕ, and T are shown in Fig. A.2, A.3, and A.4, respectively. In case of our HAPD, F is so small that we have no drastic dependence on F. As for ϕ and T, emission rate is almost proportional to $\exp(-\phi/kT)$. The slope of the plot in Fig. A.3 is almost proportional to $-1/kT$. The slope of the plot in Fig. A.4 is steeper at larger ϕ.

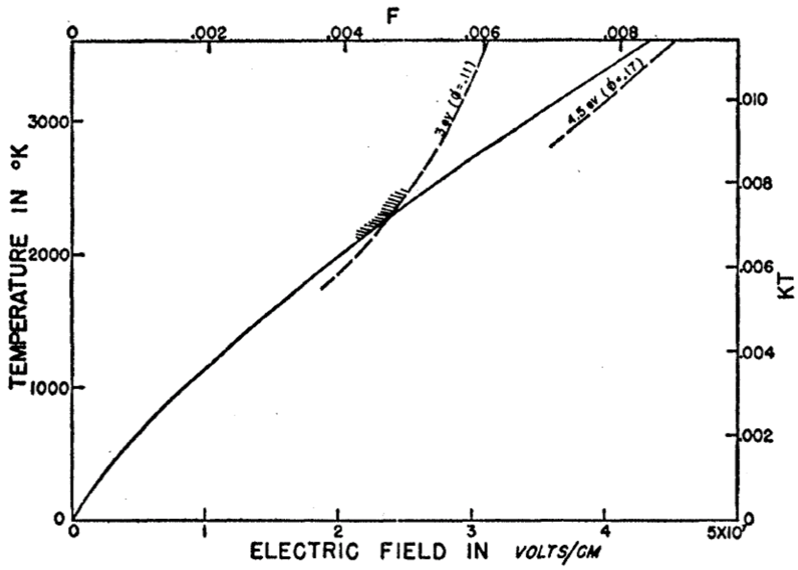

Figure A.1: Boundaries of the thermionic emission region as given by Eq. (A.9), the broken lines, and by Eq. (A.10), the solid line. For a work function of 3 eV, the region extends from the temperature axis out to the first line encountered as indicated by the shading. This figure is taken from [1].

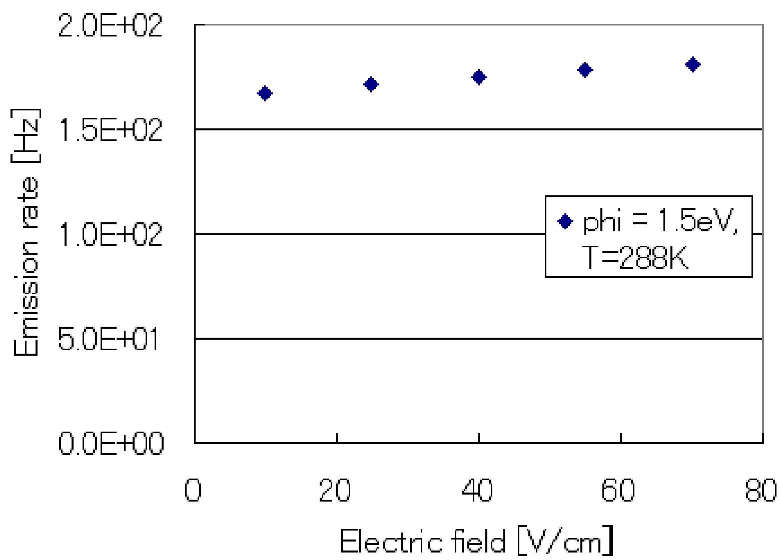

Figure A.2: The emission rate as a function of the electric field F, with T=288 K, ϕ=1.5 eV.

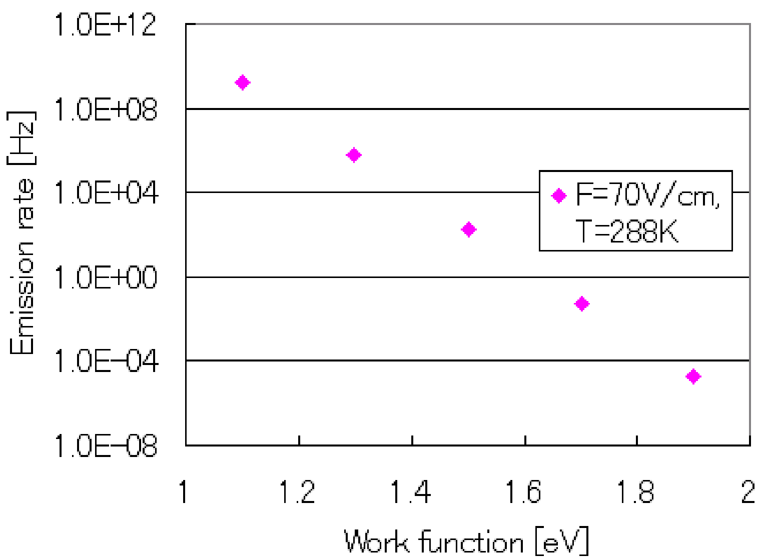

Figure A.3: The emission rate as a function of the work function ϕ, with T=288 K, F=70 V/cm.

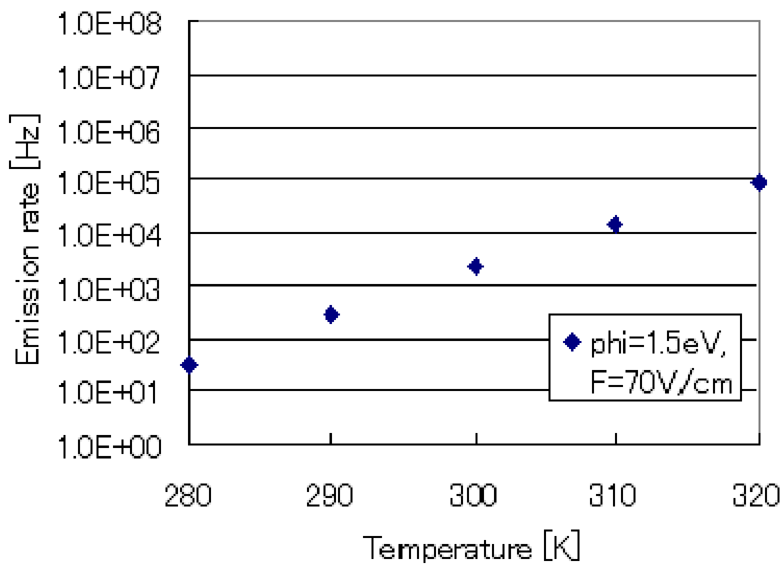

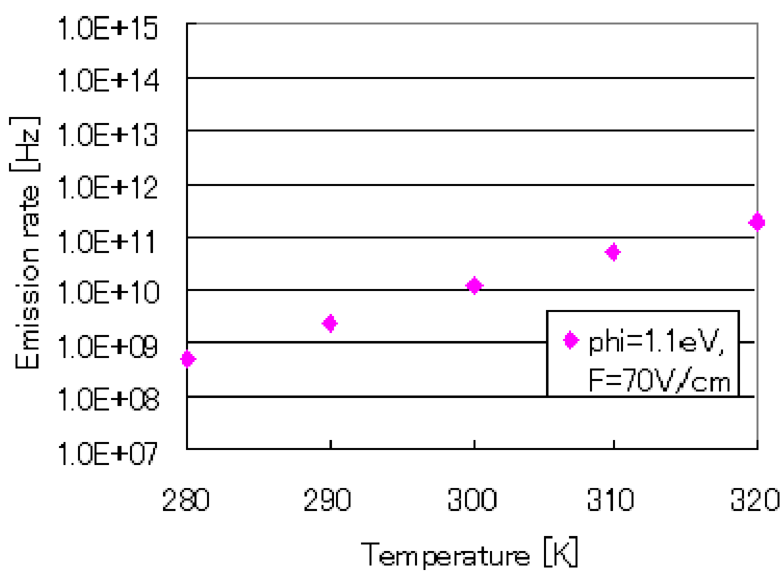

Figure A.4: The emission rate as a function of the temperature T, with F=70 V/cm, ϕ=1.5 eV(for upper figure) or 1.1 eV(for lower figure).

Appendix B

Data acquisition system in water Cherenkov detector

A possible setup of data acquisition system in the water Cherenkov detector is shown in Fig. B.1 and Fig. B.2. It is similar to the setup of Super-Kamiokane[47].

The raw signals from the HAPD is fed to an "analog input block" shown in Fig. B.1. In the analog input block, we split the signal after the preamplifier into 3 signals. One of them is fed to the analog discriminator to provide a HITSUM signal. Other two signals are fed to AMCs. Two AMCs are used so that events in rapid succession, such as a muon followed by its decay electron, can be processed without deadtime.

The HITSUM signals from all the analog input blocks are fed to "Trigger control", which decide whether we should take that event or not. If it decide to take the event, it feeds the trigger signal to all the the analog input blocks. The threshold of the discriminator should be carefully chosen, so that the trigger rate is tolerable. To reduce trigger rate, the dark count rate of the HAPD should also be low enough.

Data taking of the AMC is controlled by "channel control". Global clock which is fed to the "channel control" determines the start timing of the data taking of the AMCs. If trigger is not issued during the data taking of the AMCs, they are discharged and start data taking again by the next global clock. If trigger is issued, stored waveform is read out and fed to the FADCs. The readout speed is $2 \sim 3\,\mathrm{MHz}$ per stage, and it determines the total speed of data acquisition system. However, the deadtime of the system is significantly reduced by using two AMCs.

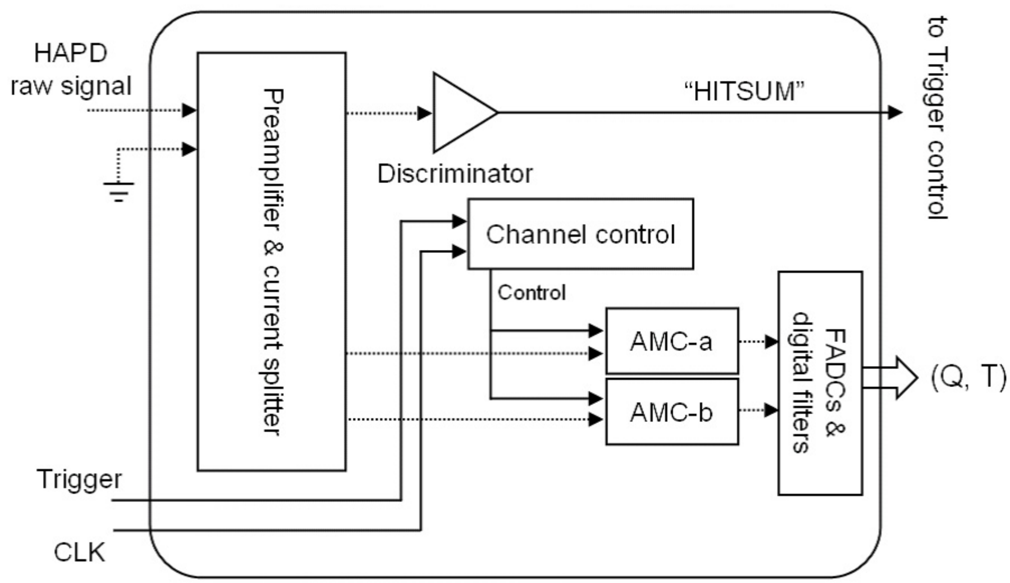

Figure B.1: A schematic view of the analog input block. Only one channel is shown in the figure. Dashed arrows show the analog signals. Solid arrows show the logic signals which control the processing of the analog signals.

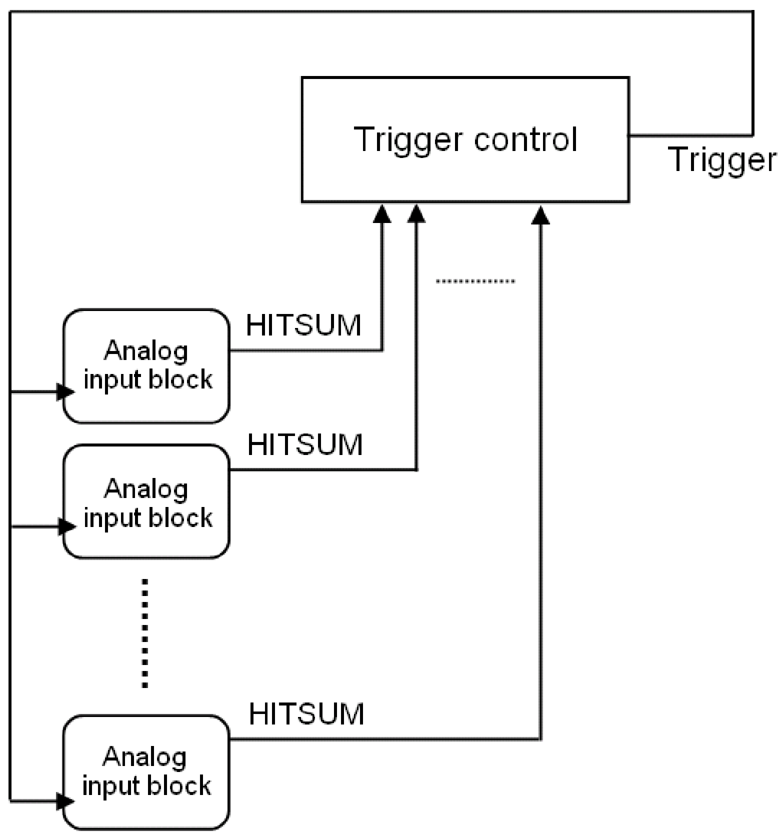

Figure B.2: The HITSUM signals from all the analog input blocks are fed to the Trigger control. Trigger control decide whether we should take that event or not. If it decide to take the event, it feeds the trigger signal to all the the analog input blocks.

Acknowledgement

I would like to express my great appreciation to my supervisor Prof. H. Aihara, for his overall support and useful suggestions. I greatly acknowledge M. Iwasaki, H. Kakuno, and T. Abe, for daily discussion and useful advices.

I am indebted to Y. Kawai, M. Suyama and the other members of the electron tube center (ETC) of Hamamatsu Photonics K.K. (HPK), especially for the development of the HAPD and the preamplifiers. I am especially thankful to M. Tanaka and the other members of the KEK electronics group, especially for the development of the AMC ASIC. I would like to express my appreciation to M.Shiozawa (ICRR), especially for the physics requirements of Hyper-Kamiokande.

I am also thankful for Prof. M. Price and Prof. C. Joram (CERN) for advices about HAPD, during the CERN Summer Student Programme 2004. I really enjoyed staying at CERN.

My appreciation also goes to the members of Aihara laboratory. I would like to appreciate A. Kusaka, for his pioneering research. I also thank K. Tanabe, R. Ishida, K. Ito, Y. Nakahama, K. Yamada, T. Nakadaira, H. Kawai, for a nice life in Hongo.

Finally I would like to express my great appreciation to my parents.

Bibliography

[1] E. L. Murphy and R. H. Good, Jr., "Thermionic emission, field emission, and the transition region," *Phys. Rev.* **102** (1956) 1464–1473.

[2] **Super-Kamiokande** Collaboration, Y. Fukuda *et al.*, "Evidence for oscillation of atmospheric neutrinos," *Phys. Rev. Lett.* **81** (1998) 1562–1567, `hep-ex/9807003`.

[3] **Super-Kamiokande** Collaboration, S. Fukuda *et al.*, "Determination of solar neutrino oscillation parameters using 1496 days of super-kamiokande-i data," *Phys. Lett.* **B539** (2002) 179–187, `hep-ex/0205075`.

[4] **Super-Kamiokande** Collaboration, M. Nakahata, "Super-kamiokande's solar neutrino results," *Nucl. Phys. Proc. Suppl.* **143** (2005) 13–20.

[5] **SNO** Collaboration, Q. R. Ahmad *et al.*, "Direct evidence for neutrino flavor transformation from neutral-current interactions in the sudbury neutrino observatory," *Phys. Rev. Lett.* **89** (2002) 011301, `nucl-ex/0204008`.

[6] **SNO** Collaboration, B. Aharmim *et al.*, "Electron antineutrino search at the sudbury neutrino observatory," *Phys. Rev.* **D70** (2004) 093014, `hep-ex/0407029`.

[7] **KamLAND** Collaboration, K. Eguchi *et al.*, "First results from KamLAND: Evidence for reactor anti-neutrino disappearance," *Phys. Rev. Lett.* **90** (2003) 021802, `hep-ex/0212021`.

[8] **KamLAND** Collaboration, K. Eguchi *et al.*, "A high sensitivity search for anti-nu/e's from the sun and other sources at kamland," *Phys. Rev. Lett.* **92** (2004) 071301, `hep-ex/0310047`.

[9] **KamLAND** Collaboration, T. Araki *et al.*, "Measurement of neutrino oscillation with kamland: Evidence of spectral distortion," *Phys. Rev. Lett.* **94** (2005) 081801, `hep-ex/0406035`.

[10] **KamLAND** Collaboration, M. P. Decowski, "Measurement of anti-neutrino spectral distortion by kamland," *Int. J. Mod. Phys.* **A20** (2005) 3051–3054.

[11] K. Nakamura, “Hyper-Kamiokande — A next generation water Cerenkov detector,” *Int. J. Mod. Phys.* **A18** (2003) 4053–4063.

[12] **Super-Kamiokande** Collaboration, Y. Ashie *et al.*, “Evidence for an oscillatory signature in atmospheric neutrino oscillation,” *Phys. Rev. Lett.* **93** (2004) 101801, `hep-ex/0404034`.

[13] **K2K** Collaboration, E. Aliu *et al.*, “Evidence for muon neutrino oscillation in an accelerator- based experiment,” *Phys. Rev. Lett.* **94** (2005) 081802, `hep-ex/0411038`.

[14] **Super-Kamiokande** Collaboration, M. Shiozawa *et al.*, “Search for proton decay via p -> e+ pi0 in a large water cherenkov detector,” *Phys. Rev. Lett.* **81** (1998) 3319–3323, `hep-ex/9806014`.

[15] **Super-Kamiokande** Collaboration, Y. Hayato *et al.*, “Search for proton decay through p -> anti-nu k+ in a large water cherenkov detector,” *Phys. Rev. Lett.* **83** (1999) 1529–1533, `hep-ex/9904020`.

[16] **Super-Kamiokande** Collaboration, K. Kobayashi *et al.*, “Search for nucleon decay via modes favored by supersymmetric grand unification models in super- kamiokande-i,” *Phys. Rev.* **D72** (2005) 052007, `hep-ex/0502026`.

[17] “Letter of Intent, Neutrino oscillation experiment at JHF,” January, 2003. `http://www-nu.kek.jp/jhfnu/index_e.html`.

[18] F. A. White and J. C. Sheffield, “Reversed-biased P-N junctions in electron tubes,” *Proc. IRE* **50** (1962), no. 6, 1523–1524.

[19] R. DeSalvo, “Hybrid photodiode tube,”. CLNS-87-92.

[20] L. K. van Geest and K. W. J. Stoop, “Hybrid phototube with Si target,” *Nucl. Instrum. Meth.* **A310** (1991) 261–266.

[21] T. Gys, “The pixel hybrid photon detectors for the LHCb-RICH project,” *Nucl. Instrum. Meth.* **A465** (2000) 240–246.

[22] A. Braem *et al.*, “Development of large area hybrid photodiodes for the LHCb ring imaging Cherenkov detectors,” *IEEE Trans. Nucl. Sci.* **46** (1999) 365–370.

[23] P. Cushman *et al.*, “Multi-pixel hybrid photodiode tubes for the CMS hadron calorimeter,” *Nucl. Instrum. Meth.* **A387** (1997) 107–112.

[24] A. Piccioli *et al.*, “Hpd imaging properties in cherenkov telescopes,” *Nucl. Instrum. Meth.* **A525** (2004) 144–147.

[25] M. Suyama *et al.*, “Fundamental investigation of vacuum PD tube [photodiode],” *IEEE Trans. Nucl. Sci.* **41** (1994) 719–724.

[26] M. Suyama *et al.*, “A compact hybrid photodetector (HPD),” *IEEE Trans. Nucl. Sci.* **44** (1997) 985–989.

[27] M. Suyama *et al.*, “A hybrid photodetector (HPD) with a III-V photocathode,” *IEEE Trans. Nucl. Sci.* **45** (1998) 572–575.

[28] N. Kanaya *et al.*, “Test results on hybrid photodiodes,” *Nucl. Instrum. Meth.* **A421** (1999) 512–521.

[29] Hamamatsu Photonics K. K., “HPD (Hybrid Photo-Detector) Modules H8236-07/40.”. `http://www.hamamatsu.com/`.

[30] S. M. Bradbury, R. Mirzoian, J. Gebauer, E. Feigl, and E. Lorenz, “Test of the new hybrid INTEVAC intensified photocell for the use in air Cerenkov telescopes,” *Nucl. Instrum. Meth.* **A387** (1997) 45–49.

[31] R. Mirzoyan, D. Ferenc, and E. Lorenz, “An evaluation of the new compact hybrid photodiodes R7110U-07/40 from Hamamatsu in high-speed light detection mode,” *Nucl. Instrum. Meth.* **A442** (2000) 140–145.

[32] M. Akatsu *et al.*, “Time-of-propagation Cherenkov counter for particle identification,” *Nucl. Instrum. Meth.* **A440** (2000) 124–135, `physics/9904009`.

[33] S. Matsui *et al.*, “HAPD time-resolution study under single-photon irradiation,” *Nucl. Instrum. Meth.* **A463** (2001) 220–226.

[34] N. Kanaya, “HPD for linear colliders,” *Nucl. Instrum. Meth.* **A442** (2000) 295–299.

[35] A. Kusaka, “Research and development of a hybrid photo sensor for a water cerenkov detector,” 2004.

[36] M. Suyama, “Development of a multi-pixel photon sensor with single-photon sensitivity,”. KEK-REPORT-2002-16.

[37] M. Suyama *et al.*, “Development of a multi-pixel photon sensor with single-photon sensitivity,” *Nucl. Instrum. Meth.* **A523** (2004) 147–157, `physics/0312017`.

[38] M. Suyama *et al.*, “Development of a multi-pixel hybrid photo-detector with high quantum efficiency and gain,” *IEEE Trans. Nucl. Sci.* **51** (2004) 1056–1059, `physics/0402126`.

[39] Hamamatsu Photonics K. K., “Large photocathode area photomoltiplier tubes.”. `http://www.hamamatsu.com/`.

[40] H. Kume *et al.*, “20 inch diameter photomultiplier,” *Nucl. Instrum. Meth.* **205** (1983) 443–449.

[41] A. Suzuki *et al.*, “Improvement of 20-inch diameter photomultiplier tubes,” *Nucl. Instrum. Meth.* **A329** (1993) 299–313.

[42] K. Arisaka, “Principle of PMT and its calibration,” September, 2005. Lecture note at UCLA.
`http://www.physics.ucla.edu/~arisaka/auger/energy/pmt_basics.pdf`.

[43] K. Deiters *et al.*, “Properties of the most recent avalanche photodiodes for the CMS electromagnetic calorimeter,” *Nucl. Instrum. Meth.* **A442** (2000) 193–197.

[44] K. Deiters *et al.*, “Properties of the avalanche photodiodes for the CMS electromagnetic calorimeter,” *Nucl. Instrum. Meth.* **A453** (2000) 223–226.

[45] M. Tanaka, H. Ikeda, K. Tamai, M. Takemoto, and H. Hayashii, “Development and evaluation of charge sensitive preamplifier for CsI calorimeter in the KEK B factory,” *IEEE Trans. Nucl. Sci.* **41** (1994) 1208–1211.

[46] Xilinx, Inc., “”Xilinx LogiCORE ”Distributed Arithmetic FIR Filter”.”.
`http://www.xilinx.com/ipcenter/catalog/logicore/docs/da_fir.pdf`.

[47] Y. Fukuda *et al.*, “The super-kamiokande detector,” *Nucl. Instrum. Meth.* **A501** (2003) 418–462.